NOISE CHARACTERIZATION AND DEVICE MODELLING
OF QUANTUM WELL INFRARED PHOTODETECTORS

BY

DANIEL CHIEN WANG

A DISSERTATION PRESENTED TO THE GRADUATE SCHOOL OF
THE UNIVERSITY OF FLORIDA IN PARTIAL FULFILLMENT
OF THE REQUIREMENTS FOR THE DEGREE OF
DOCTOR OF PHILOSOPHY

UNIVERSITY OF FLORIDA

1996

ACKNOWLEDGEMENTS

TABLE OF CONTENTS

NOISE CHARACTERIZATION AND DEVICE MODELLING
OF QUANTUM WELL INFRARED PHOTODETECTORS

By

Daniel C. Wang

May 1996

A complete DC and noise characterization of III-V semiconductor quantum well infrared photodetectors (QWIPs) designed for 8-12μm infrared detection is presented. These devices consist of multiple periods of quantum well and superlattice or bulk barrier layers grown by Molecular Beam Epitaxy (MBE) technique using GaAs and InP based ternary compound semiconductor materials. Photodetection is based on photon induced electron or hole intersubband transitions between the localized ground states inside the quantum wells and the continuous, non-localized states of the bulk barrier layers or miniband of superlattice barrier layers, respectively.

The dark current of n-type miniband QWIPs has been modelled using a modified thermionic emission theory and takes into account Schottky image barrier lowering effect. The agreement between the current model and the DC characteristics of the device indicates that the charge transport process is emission limited for these n-type miniband QWIPs. In addition, both n-type and p-type device operation under low applied bias voltage has been examined. Under low electric fields and at low

temperatures, the device can be described as M statistically independent sections in series, where M is equal to the ratio of active device length over the extended state carrier trajectory. The excellent agreement between the measured and calculated dark current-voltage characteristics confirms this model.

Dark current noise measurements between 10^1 and 10^5 Hz were carried out on both n-type miniband and p-type strained layer QWIPs as a function of temperature and bias voltage. The observed noise can be attributed to number fluctuation noise associated with the generation and recombination of electrons or holes from and to the quantum well bound states and the extended miniband or valence band states. At low bias the number fluctuation noise translates into current fluctuation noise via electron or hole diffusion, whereas at higher bias values the coupling is via the electron or hole drift current component. From the measured noise data of the n-type miniband QWIPs, the low-bias electron diffusion length, the bias-dependent noise gain, the electron trapping probability and the thermal electron generation rate are determined. From the noise data of p-type QWIPs, the value for the capture coefficient of hole trapping is determined and interpreted in terms of the Be-acceptor characteristics. We observed that the thermally generated heavy holes diffuse, at low fields, on the average to the nearest neighboring quantum well where they subsequently recombine.

Design criteria are proposed based on maximizing the detectivity of the QWIP. Using the noise model and a simplified absorption coefficient expression, the detectivity can be calculated as a function of the number and doping concentration of the quantum wells and the effective masses of electrons and holes in the quantum wells.

CHAPTER 1
INTRODUCTION

1.1   Infrared Photodetectors

Methods to detect infrared (IR) radiation have been studied ever since its discovery by William Herschel in 1800[1]. Among the various kinds of infrared detectors, those responding to radiation in the wavelength regions of 1-3 μm, 3-5 μm and 8-14 μm (the so-called atmospheric windows) receive most attention. Detectors operating in the wavelength region of 8-14 μm are especially important for imaging since the temperature of the human body and environments suitable for human life are around 300 K, which has a emission peak wavelength at 10 μm in their radiation spectrum. Various detectors have been designed and fabricated. Most of them fall into one of the two general classes: 1) thermal detectors which register the temperature dependent properties of the detecting elements to sense the temperature variation caused by the IR radiation, and 2) photon detectors which detect the change in the electronic state of the detectors subjected to the IR radiation.

Although thermal detectors have the important practical advantage that they can be used at ambient temperatures thus eliminating the need for cryogenic cooling systems, their poor sensitivities and slow response times compared to photon detectors (typically two orders of magnitude lower in terms of detectivity D*) limit their usage. In contrast, despite the complexity of cooling systems, the performance of photon detectors is high and continues to improve because of the development of highly purified, single-crystal semiconductors used as active material. However, there are

1

still some problems among the various kinds of photon detectors: For example, a poor quantum efficiency of PtSi and IrSi Schottky barrier detectors in the 8-14μm spectral regime, inferior noise characteristics and limited usable storage capacity due to a fairly high gate voltage of MIS detectors, and a relatively low absorption coefficient for selectively doped silicon or germanium extrinsic photoconductive detectors. In Mercury Cadmium Telluride (MCT) detectors which have the highest detectivity among IR detectors, material softness and non-uniformity are still a major obstacle for the Focal Plane Array (FPA) applications.

1.2 Quantum Well Infrared Photodetectors

Since West and Eglash first observed infrared absorption resulting from an intersubband transition in a GaAs/AlGaAs quantum well structure[2], quantum well infrared detectors (QWIPs) have become increasingly popular. Using molecular beam epitaxy (MBE) and metal organic chemical vapor deposition (MOCVD) techniques, the dimensional control of the potential profile and impurity distribution approaches the scale of interatomic spacing with very low interface state densities ($< 10^{10}/cm^2$). The available material systems include III-V, II-VI, IV-VI compound and elemental semiconductors. Many publications have appeared discussing the structure, performance and feasibility of the QWIPs[3]–[57]. Despite the large dark current in comparison with a $Hg_{1-x}Cd_xTe$ (MCT) detector, a QWIP has higher production yield, better area uniformity, lower fabrication cost, and fewer material defects than MCT detectors, and provides energy band selectivity and a predictable spectral response. All these advantages make QWIPs good candidates for 8-14μm long wavelength infrared detection.

It is predicted theoretically that the dark current of a n-type QWIP based on the intersubband transition in GaAs/GaAlAs is always several orders of magnitude higher than that of a MCT detector at the same cutoff wavelength and operating

temperature. This is due to the fact that the QWIP is a majority carrier device and its dark current is determined mainly by the thermally generated carriers. In general, the higher the dark current of a QWIP, the higher its noise current will be. Since detectivity is directly related to the noise current, many different novel QWIP structures with lower dark current characteristics have been proposed to improve the performance in terms of detectivity[16]. P-type QWIPs were expected to have better noise characteristics because of the higher effective mass and larger density of states of the holes resulting in a lower dark current[17]–[21]. Due to the mixing between the light- and heavy-hole states, normal incident illumination produces an intersubband transition in p-type QWIPs, and thus eliminates the need for grating structures. This feature is another reason for studying p-type QWIPs even though their absorption coefficients are somewhat lower than those of n-type QWIPs.

In order to optimize QWIP device performance, an understanding of both transport and optical properties is required. The commonly used models which describe these properties are presented in the following three sections.

1.3 Dark Current Calculation

L. Esaki first introduced the multi quantum well concept for photodetector applications. He calculated the tunneling current in a finite superlattice structure[15]

$$J = \frac{em^*kT}{2\pi^2\hbar^2} \int_0^\infty T^*T \cdot ln\left(\frac{1 + exp[(E_f - E_t)/kT]}{1 + exp[(E_f - E_t - eV)/kT]}\right) dE_t \qquad (1.1)$$

where T^*T is the transmission probability for a conducting carrier tunneling through the superlattice energy barrier.

Esaki's approach was successful in modeling a simple superlattice structure without doping in the quantum wells. For the recently developed QWIPs with highly doped quantum wells this theory needs to be modified.

B. F. Levine has published a series of papers dealing with the characteristics of the QWIP. His dark current expression is based on the scattering mechanism[7] that[7]

$$I_d(V) = n(V)evA \qquad (1.2)$$

where $n(V)$ is the effective density of electrons, which can be calculated by

$$n(V) = \left(\frac{m^*}{\pi \hbar^2 L_p}\right) \int_{E_0}^{\infty} f(E)T(E,V)dE \qquad (1.3)$$

where L_p is the width of the quantum well, and $T(E,v)$ is the electron transmission probability for tunnelling through the quantum well barrier. The velocity used in Levine's dark current expression was given by the empirical velocity electric field relation,

$$v = \mu F[1 + (\mu F/v_s)^2]^{-1/2} \qquad (1.4)$$

where μ is the mobility, F is the average electric field, and v_s is the saturation drift velocity.

The above expression for the dark current has been widely used to describe the voltage-current characteristics of a QWIP in many publications[23]–[26]. Unfortunately, mixed scattering mechanism with ballistic transport in this approach has no physical basis and leads to internal inconsistency. A detailed discussion of this topic will be presented in chapter 2.

1.4 Photocurrent Mechanism

The operation of QWIPs is based upon the carrier's intersubband transition initiated by an impinging IR radiation. The application of an external electric field in the perpendicular transport direction will sweep the carriers toward the collecting contact and a photocurrent will be recorded.

The carrier generation rate G due to the IR radiation can be expressed as

$$G = \phi \cdot \eta \qquad (1.5)$$

where ϕ is the IR photon flux and eta is the quantum efficiency for a single carrier. Assuming that the carrier lasts an average of τ seconds before it is trapped into a quantum well, τ is called the lifetime of a photogenerated carrier in the QWIP. The average number of excited carriers N_c can be found from the product of the generation rate and the lifetime

$$N_c = G \cdot \tau = \phi \cdot \eta \cdot \tau \tag{1.6}$$

The carriers drift under the applied electric field with a velocity v_d. The contribution of each carrier to the current flowing in the external circuit is

$$i_c = q \cdot \frac{v_d}{L} \tag{1.7}$$

where q is the charge of the carrier and L is the distance between electrodes. If we define the transit time of a QWIP by $\tau_d = L/v_d$, then the total average photocurrent becomes

$$I_{(photo)} = N_c i_c = q\phi\eta \left(\frac{\tau}{\tau_d} \right) \tag{1.8}$$

Obviously, a longer carrier lifetime produces a larger photocurrent in the QWIP. We define the photocurrent gain as $g_{(photo)} \equiv \tau/\tau_d$ and the photocurrent can be expressed by

$$I_{(photo)} = q\phi\eta g_{(photo)} \tag{1.9}$$

Consider a QWIP with N quantum wells, and a potential profile as shown in Fig. 1.1, where the symbol p represents the electron trapping probability for the excited carriers in the quantum well states. Thus, $(1 - p)$ is the probability that electrons travel through the well region. If we assume that (a) the photon flux is independent of position, (b) the dark current is limited by thermal effects and interwell tunneling may be neglected, and (c) the ohmic contacts in the QWIPs are ideal contacts, then the photo current i_m at each barrier m can be expressed as[24]

$$
\begin{aligned}
i_{m+1} &= (1-p)i_m + photocurrent\ generated\ from\ one\ well \\
&= (1-p)i_m + q\phi\eta'(1-p) \tag{1.10}
\end{aligned}
$$

where η' is the quantum efficiency for a single well. With current continuity, $i_m = i_{(m+1)} = i(photo)$, then

$$
\begin{aligned}
i_{(photo)} &= q\phi\eta'\frac{(1-p)}{p} \\
&= q\phi\eta\frac{(1-p)}{Np} \\
&= q\phi\eta g_{(photo)}
\end{aligned}
\tag{1.11}
$$

where, the photocurrent gain, $g_{(photo)}$, is equal to

$$
g_{(photo)} = \frac{(1-p)}{Np}
\tag{1.12}
$$

1.5   Noise Mechanism

The noise associated with the dark current of a QWIP is usually controlled by trapping and detrapping processes between the extended states and the localized states inside the quantum wells. If we assume the carrier density in the extended states is N_c and in the quantum well bound state is N_s, and that the carrier lifetime in the extended states is τ_0 and in quantum well bound states is τ_s, then the particle number spectral density becomes[29]

$$
S_N(f) = 4\overline{\Delta N^2}\frac{\tau}{1+\omega^2\tau^2} = 4\beta N_c\frac{\tau}{1+\omega^2\tau^2}
\tag{1.13}
$$

where $\tau^{-1} \approx \tau_0^{-1} + \tau_s^{-1}$ and $\beta = \tau_s/(\tau_0 + \tau_s)$.

In a QWIP, the number of conducting carriers is equal to the total number of carriers excited. With the average current $\overline{I} = N_c i_c$, where i_c is the current contributed by a single carrier, the noise current spectral density can be expressed in terms of $S_N(f)$

$$
S_i(f) = i_c^2 S_N(f) = 4\overline{I}^2\frac{\beta}{N_c}\frac{\tau}{1+\omega^2\tau^2}
\tag{1.14}
$$

In equilibrium, the average number of carrier generated from the quantum well is equal to the average number of carrier recombining in the quantum wells. We have

$$
\frac{N_s}{\tau_s} = \frac{N_c}{\tau_0}
\tag{1.15}
$$

At low temperatures, the electron density in the extended states is much smaller than the electron density in the quantum well. As a result, τ_0 is much smaller than τ_s. This implies β equals one in Eq. (1.14). Using $\bar{I} = \frac{qN_s}{\tau_d}$, we can further simplify Eq. (1.14) to

$$
\begin{aligned}
S_i(f) &\approx 4q\bar{I}\frac{\frac{\tau}{\tau_d}}{1+\omega^2\tau^2} \\
&= 4q\bar{I}g\frac{1}{1+\omega^2\tau^2}
\end{aligned}
\tag{1.16}
$$

where $g = \frac{\tau}{\tau_d}$ is defined as "noise current gain" in a QWIP. In most cases, $\omega\tau \ll 1$, allowing the g-r noise current spectral density function to simplify to

$$
S_i(f) \approx 4q\bar{I}g
\tag{1.17}
$$

1.6 Outline of the Dissertation

In order to resolve the self-inconsistency in the dark current expression used by Levine, a model based on thermionic emission is presented in chapter 2. The modelled dark current is compared with the measured current for three different bound-to-miniband (BTM) transition QWIPs. In addition, an empirical current expression using a phenomenological ideality factor is also examined. The ideality factor extracted from the dynamic resistance of each QWIP was used to calculate the dark current and compared to the measured data. A better understanding of QWIP transport properties results from these studies.

Current conduction of a QWIP under low bias operation is discussed in chapter 3. The voltage-current characteristic inferred from QWIP noise characteristics under equilibrium was calculated and compared with the measured current. The good agreement between the modelled and measured data confirms our model assumption.

To evaluate the performance of a QWIP, D^* is the most often used figure of merit. To calculate the D^* at a certain frequency, the noise value at this frequency must be known. Also, to optimize the operating bias voltage for a QWIP, noise

information is required. Thus, noise measurements provide the only way to obtain all these parameters. Detailed noise measurements were carried out for three BTM QWIPs at 77K. The noise spectra of these QWIPs under different bias voltages are presented in chapter 4. By analyzing the measured g-r noise spectral density, the low bias diffusion length, the bias dependent noise gain, as well as the electron trapping probability were calculated and discussed in this chapter. The dependency of the thermal electron generation rate on external bias voltage is also verified. The increase in the electron generation rate due to an increase in the bias voltage justifies the deviation of current noise level from the I^2 dependency in high bias regions.

A noise model based on a priori known quantities was developed. Noise measurements on a p-type QWIP were performed to verify our model. The measured current noise spectra are presented in chapter 5 for different temperatures and bias voltages. Two different regimes of operation were identified from the noise spectra. Based upon this model, low field hole diffusion length as well as the capture cross-section for hole trapping were extracted from the noise data.

Using our noise model and a simplified quantum efficiency expression, the detectivity can be derived as a function of design parameters. The dependency on three different design parameters namely, number of quantum wells, doping concentration, and the effective mass were examined for a p-type QWIP and presented in chapter 6 to investigate the results of parameter optimization. Design criteria are stated at the end of this chapter as a guideline for a QWIP designer.

Finally, chapter 7 contains the summary, conclusions, and recommendations for future research.
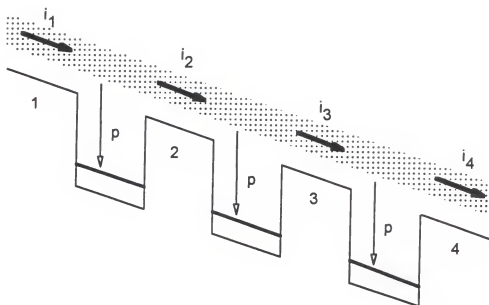
Figure 1.1 Energy band diagram of a QWIP with a constant electric field..

CHAPTER 2
N-TYPE QWIP DARK CURRENT CHARACTERISTICS

2.1 Introduction

Understanding the dark current in a QWIP is one of the most important aspects for optimizing detector performance. Several publications have addressed and modeled the dark current[22]–[27]. Unfortunately, most of the calculations are based on the electron's velocity-field relationship, which is empirical and takes scattering mechanisms into account. There is nothing wrong with modeling the dark current based on the empirical velocity expression, $v = \mu F[1 + (\mu F/v_s)^2]^{-1/2}$. The problem is the electron density, n, which is calculated by inserting the tunneling transmission coefficient, $T(E,V)$, into the Fermi integral in most of the dark current expressions[7],

$$n(V) = \left(\frac{m^*}{\pi \hbar^2 L_p}\right) \int_{E_0}^{\infty} f(E)T(E,V)dE$$

As we know, the transmission coefficient is derived for an elastic process which implies that the electrons should experience ballistic transport. Obviously, this kind of calculation is inconsistent.

In this chapter, we try to introduce a current model derived from thermionic emission coupled with the electron image lowing effect which has a better physical basis and does not involve parameter fitting in the current expression. The dark currents of three miniband QWIP structures were measured at 77K and compared with the modelled current values. In addition, an ideality factor was extracted from the dynamic resistance for each sample. The empirical current model based on the

10

ideality factor was also compared with the measured values. The results presented in this chapter give a better explanation for the QWIP's transport characteristics.

2.2 Dark Current Modelling

2.2.1 Thermionic emission theory

For a QWIP with highly doped quantum wells, which behaves in some aspects similar to a metal, thermionic emission theory may apply. For a miniband QWIP with one bound state E_1 inside the quantum wells, the density of states can be approximated as

$$g(E) = \begin{cases} 0 & E < E_1 \\ \frac{m^*}{\pi \hbar^2 L_w} & E_1 \leq E < E_{mb} \\ \frac{m^*}{\pi \hbar^2 L_w} + \frac{4\pi(2m^*)^{3/2}}{h^3}(E - E_{mb})^{1/2} & E_{mb} \leq E < E_{mt} \end{cases} \qquad (2.1)$$

where E_{mb} is the bottom energy level of the miniband, E_{mt} is the highest energy level of the miniband, L_w is the width of the quantum wells, and m^* is the effective mass of the carriers in the quantum wells.

The kinetic energy of an electron inside the miniband is $\frac{1}{2}m^*(v_x^2 + v_y^2 + v_z^2) = E - E_{mb}$. For miniband transport, only an electron which has momentum in the z direction can contribute to the current. If we neglect the current contributing of electrons with energy larger than E_{mt}, the thermionic emission current density is given by

$$\begin{aligned} J_{th} &= \int e v_z dn \\ &= \int_{E_{mb}}^{E_{mt}} e v_z \frac{4\pi(2m^*)^{3/2}}{h^3}(E - E_{mb})^{1/2} f(E) dE \end{aligned} \qquad (2.2)$$

where $f(E)$ is the Fermi-distribution function. Since the fermi level is far below E_{mb} for the miniband QWIPs, we can simplify $f(E)$ to a Boltzman-distribution resulting in

$$J_{th} = e\frac{4\pi m^* k^2 T^2}{h^3}\exp(-\frac{qV_n}{kT})\left[1-\exp(-\frac{E_{mt}-E_{mb}}{kT})\right]$$

$$= A^* T^2 \exp(-\frac{qV_n}{kT})\left[1-\exp(-\frac{E_{mt}-E_{mb}}{kT})\right] \tag{2.3}$$

where $qV_n = E_{mb} - E_f$ and A^* is the effective Richardson constant for the thermionic emission.

2.2.2 Schottky effect

In a QWIP, the highly doped quantum wells act similar to metal. Therefore, the image-force-induced lowering of the potential energy need to be taken into account. Consider the following situation: When an electron is in the barrier region at a distance x from the quantum-well/barrier interface, a positive charge will be induced at this interface surface. The image force is given by[34]

$$F = \frac{-e^2}{4\pi(2x)^2\epsilon_r\epsilon_0} = \frac{-e^2}{16\pi\epsilon_r\epsilon_0 x^2} \tag{2.4}$$

where $-e$ is the electron charge, ϵ_r is the dielectric constant of the barrier, and ϵ_0 is the permittivity in vacuum. When an external field $\mathcal{E}$ is applied, the total potential energy PE as a function of distance (taken $PE(x \to \infty)|_{\mathcal{E}=0} = 0$) is

$$PE(x) = \frac{-e^2}{16\pi\epsilon x} - e\mathcal{E}x \tag{2.5}$$

The Schottky barrier lowering $e\Delta\phi$ is given by the condition $\frac{d[PE(x)]}{dx} = 0$, which results in

$$e\Delta\phi = e\sqrt{\frac{e\mathcal{E}}{4\pi\epsilon_r\epsilon_0}} \tag{2.6}$$

Therefore, the effective barrier height is reduced to

$$E_{b,eff} = E_{mb} - e\Delta\phi \tag{2.7}$$

Figure 2.1 shows the energy band diagram of a miniband QWIP when an external reverse bias voltage is applied.

To have a significant Schottky effect, electrons inside the conducting material must have sufficient time to form a charge plane (image plane) during electron escape[23]. Therefore, the dielectric relaxation time, τ_{rel}, in the Fermi sea must be much smaller than the electron escape time, τ_{esc}, i.e.,

$$\tau_{esc} \gg \tau_{rel} = \epsilon_r \epsilon_0 \rho = \frac{\epsilon_r \epsilon_0}{e \mu n} \tag{2.8}$$

where ρ is the resistivity, ϵ_r is the dielectric constant, μ is the electron mobility for the conducting material, and n is the electron density. For a GaAs quantum well with doping density 5×10^{17} cm^{-3}, the dielectric relaxation time is 7×10^{-17} $sec.$ at 77K assuming that dopants inside the quantum well are fully ionized. On the other hand, the escape time can be estimated from the time it takes an electron to pass through a single barrier. If we approximate the electron average velocity by

$$\overline{v} = \sqrt{\frac{3kT}{m^*}} \tag{2.9}$$

The escape time can be written as

$$\tau_{esc} \approx \frac{L_b}{\overline{v}} \tag{2.10}$$

For a GaAs barrier with barrier width 500 Å, the escape time is approximately 2.2×10^{-13} $sec.$ at 77K. The above first order calculation shows that τ_{rel} is significantly smaller than τ_{esc} indicating that indeed the Schottky effect needs to be accounted for.

2.2.3 Two sided current approach

Let us consider a superlattice barrier with doped quantum wells on both side. When a reverse bias voltage is applied, the barrier height will be lowered by an amount of $e\Delta\phi$ due to the image force.

$$qV_n' = E_{mb,eff} - E_f = E_{mb} - e\Delta\phi - E_f \tag{2.11}$$

Since the magnitude of the electric field in the highly doped quantum well is negligible, all the voltage will drop across the barrier region. The electron current density generated from the left side quantum well to the mini-band becomes

$$J_l = A^* T^2 \exp(-\frac{qV_n'}{kT}) \left[1 - \exp(-\frac{E_{mt} - E_{mb,eff}}{kT})\right] \qquad (2.12)$$

The current density for right side quantum well to the miniband becomes

$$J_r = A^* T^2 \exp(-\frac{qV_n' + eV}{kT}) \left[1 - \exp(-\frac{E_{mt} - E_{mb,eff}}{kT})\right] \qquad (2.13)$$

The thermal emission current density for both directions is shown in Fig. 2.1. With these two opposing currents J_l and J_r, the total current density becomes

$$
\begin{aligned}
J &= J_l - J_r \\
&= A^* T^2 \exp(-\frac{qV_n'}{kT}) \left[1 - \exp(-\frac{E_{mt} - E_{mb,eff}}{kT})\right] \left[1 - \exp(-\frac{eV}{kT})\right] \\
&= J_s[1 - \exp(-\frac{eV}{kT})] \qquad (2.14)
\end{aligned}
$$

2.3 Fermi Level Calculation

In our dark current expression, the only unknown parameter is the Fermi energy E_f. In this section, the Fermi energy is calculated based on charge neutrality in equilibrium. The effect of doping overshoot caused by the imperfection of MBE growth is also taken into account in the Fermi level calculation.

2.3.1 Fermi level inside the doped quantum well

If the dopant inside the quantum well has energy level E_D then, the density of neutral donors is given by[35]

$$N_D^0 = N_D f(E_D) = \frac{N_D}{1 + \frac{1}{g_D} \exp(\frac{E_D - E_f}{kT})} \qquad (2.15)$$

where g_D is the ground-state degeneracy for the donor impurity level and is equal to two.

To preserve charge neutrality the total number of negative charges must equal the total number of positive charges. If the doping concentration is high, most of the electrons are contributed by donors, i.e., thermal band to band generation may be neglected. Then

$$N_D = N_D^0 + n \tag{2.16}$$

The electron density can be derived from Eq. (2.15) and Eq. (2.16).

$$n = \frac{N_D}{1 + g_D \exp(\frac{E_I - E_D}{kT})} \tag{2.17}$$

In a QWIP, the total number of electrons in the quantum well bound states and conduction extended states should be equal to the total number of electrons originating from the donor states.

$$\frac{N_D A L_w}{1 + g_D \exp(\frac{E_I - E_D}{kT})} = A L_w \int g_1(E) f(E) dE + A(L_b + L_w) \int g_2(E) f(E) dE \tag{2.18}$$

where L_b is the width of the barrier, A is the cross sectional area of the QWIP, and g_1, g_2 are described in Eq. (2.1)

$$
\begin{aligned}
g_1 &= \frac{m^*}{\pi \hbar^2 L_z} \\
g_2 &= \frac{4\pi(2m^*)^{3/2}}{h^3}(E - E_{mb})^{1/2}
\end{aligned}
$$

g_1 is the density of states for the bound states, g_2 is the density of states for the extended states.

Carrier confinement along the growth axis decreases the donor binding energy from the bulk value. From Bastard's paper[36], we found that the position of the donor level with respect to the ground state becomes constant for an electron sheet density larger than 10^{12} cm^{-2}. In the QWIPs we measured, the electron sheet density is always larger than this value. By using Bastard's result, we found that E_D lies 1 meV below the quantum well ground state. With this approximation, the Fermi level can be calculated.

2.3.2 Depth of dopant overshoot

It is well known that the Si dopant undergoes migration towards the surface during MBE growth. As a result of this asymmetrical dopant ion segregation into the "top-side" barrier, and the barrier energy will be pulled down by an amount $e\phi$ in the forward bias direction.

$$E_{b_F} = E_b - e\phi \tag{2.19}$$

where $E_b = E_{mb} - E_1$. Figure 2.2 shows the potential profiles of a QWIP under both equilibrium and forward bias condition. This doping migration during MBE growth results in the QWIP having an asymmetrical dark current when the external voltage is applied using opposite polarities.

As discussed in section 2.2, the dark current is proportional to the effective barrier height. The potential pull down, ϕ, of the forward bias direction can be calculated from the ratio of forward bias current and reverse bias current under high applied bias voltage.

$$\frac{I_F}{I_R} = \exp\left(\frac{e\phi}{kT}\right) \tag{2.20}$$

The dopants located in the barrier region are fully ionized because the Fermi level is much lower than the donor level. From Poisson's equation, by assuming a step doping profile in the barrier region with a width W, we have

$$-\frac{\partial^2 V}{\partial x^2} = \frac{eN_D}{\epsilon_r \epsilon_0} \quad for\ 0 < x \le W \tag{2.21}$$

where ϵ_r is the dielectric constant of the barrier. If the electric field can be neglected for $x > W$, which is approximately true, we find

$$\mathcal{E}(x) = \frac{eN_D}{\epsilon_r \epsilon_0}(x - W) \quad for\ 0 < x \le W \tag{2.22}$$

The barrier pull down can be derived by integration the electric field from 0 to W.

$$\phi = |\int_0^W \mathcal{E}(x)dx| = \frac{eN_D}{\epsilon_r \epsilon_0}\frac{W^2}{2} \tag{2.23}$$

Therefore, the doping overshoot width can be calculated from the measured dark current data.

2.3.3 Fermi level modification

Since the dopants in the barriers are fully ionized, the electrons inside the quantum well must originate from both well dopants and barrier dopants. The total electron density, therefore, becomes

$$n = \frac{N_D}{1 + g_D \exp(\frac{E_f - E_D}{kT})} + \frac{W}{L_w} N_D \tag{2.24}$$

From detailed balance, the total number of electrons should be conserved. As a result, the Fermi level has to satisfy the following equation:

$$\frac{N_D A L_w}{1 + g_D \exp(\frac{E_f - E_D}{kT})} + \frac{W}{L_w} N_D A L_w$$
$$= A L_w \int g_1(E) f(E) dE + A(L_w + L_b) \int g_2(E) f(E) dE \tag{2.25}$$

2.4 Results of Dark Current Calculation

Using the method introduced in section 2.3, the Fermi level and dopant overshoot depth were calculated. Table 2.1 shows the parameters for the measured QWIPs. Table 2.2 shows the energy band parameters and the results of the Fermi level calculation.

Due to high forward bias dark current of QWIP-A, we could not apply a reasonable high forward bias voltage to measure I_F. By comparing the measured reverse bias dark current with the current value calculated from our model, the doping overshoot W was estimated to be 106Å resulting in a forward bias potential pull down ϕ of 38 mV. With this amount of doping overshoot, the Fermi level is at 63 meV above conduction band edge. Fig. 2.3 shows the measured forward bias dark current and the modelled current assuming the barrier height equals $E_b - e\phi$. The difference

between measured and modelled currents is understandable because we assume the tunneling probability equals one for the transition from E_b to $E_b - \phi$ in our calculation. Under such a low bias voltage, the tunneling probability is much less than one which may result in an over-estimation of the forward bias current. The dark current under reverse bias voltage is shown in Fig. 2.4.

The forward bias current of QWIP-B is plotted in Fig. 2.5 and the arrows indicate the current projection when the applied bias voltage increases to infinity. Projection of the measured current is taken from a region under medium bias voltage because our current model does not include high field transport mechanisms, such as tunneling. According to this plot, the forward bias dopant overshoot was extracted to be 25Å resulting in a 2 mV forward bias potential pull down. Therefore, the Fermi level of QWIP-B lies 35 meV above the conduction band edge. Using this Fermi level value, the reverse bias current was calculated and compared to the measured dark data in Fig. 2.6. The excellent agreement between measured and modelled data supports our current model.

In QWIP-C, there seems to be no dopant overshoot. The Fermi level is calculated to be 28 meV above the conduction band edge and the forward bias dark current is shown in Fig. 2.7 for both measured and modelled current. Due to the strain effect of this QWIP, a build in potential would exist at the quantum well/barrier interface layer resulting in a decrease in the dynamic resistance when the bias voltage increases. The measured dynamic resistance of QWIP-C confirms this effect and it will be discussed in the next section. From the dynamic resistance plot in Fig. 2.13, the build in voltage, V_{bi}, is found to be 17 meV. The effect of V_{bi} is to reduce the electric field $\mathcal{E}$ resulting in a reduction of image barrier lowering. Fig. 2.8 shows the measured dark current and the modelled current for $V > 17$ mV with taking V_{bi} into account in the current calculation.

In summary, our current model is derived for an ideal QWIP. It does give a rather good estimation for the dark current value. The difference between the modelled and measured data can be attributed to effects such as the interface voltage under low field and tunneling current contributions under high field, which are not included in our current model.

2.5 Dark Current and Ideality Factor

As mentioned in the previous section, the imperfection of our current expression is caused by many non-ideal mechanisms. These effects are in general device dependent, making it hard to develop an universal model for the QWIPs. We therefore introduce an empirical ideality factor, n, to describe the dark current under low bias condition. In this section, the dark current of three QWIPs was calculated using this phenomenological concept and compared to the measured data.

2.5.1 Dynamic resistance and ideality factor

For a metal-semiconductor-metal (MSM) diode, the current can be expressed as[34]

$$I = I_s[1 - e^{\frac{-e|V|}{nkT}}] \tag{2.26}$$

where I_s is the saturation current, assumed to be independent of V, and obtained by extrapolating the current from the log-linear region to $V = 0$, and n is the ideality factor.

The band structure of the QWIP is in many ways similar to the MSM diode. The voltage applied to the QWIP $V(total)$ is equal to $N+1$ times the voltage of each period V, where N is the number of quantum wells. The dynamic resistance, r_d, can be derived from Eq. (2.26)

$$r_d = \frac{1}{\frac{dI}{dV(total)}} = (N+1)\frac{nV_T}{I_s}\exp(\frac{|V|}{nV_T}) \tag{2.27}$$

where $V_T \equiv \frac{kT}{e}$. If we plot the dynamic resistance versus bias voltage in a semi-log plot,

$$\log(r_d) = \log(\frac{(N+1)nV_T}{I_s}) + \frac{\log(e)}{nV_T} \cdot V \tag{2.28}$$

The term $\log(r_d)$ is a linear function of applied voltage V. Using Eq. (2.28), the ideality factor n can be extracted from the slope $\frac{\log(e)}{nV_T}$. Once the value of n is extracted, the saturation current I_s can be calculated from the offset $\log(\frac{(N+1)nV_T}{I_s})$ for $V = 0$.

2.5.2 Dark current calculation using the extracted ideality factor

Ideally, the saturation current I_s in Eq. (2.26) should be a constant. But in reality, I_s will increase with increasing bias voltage due to effects such as the image barrier lowering and tunnelling. As a result, the current expression based on the ideality factor can only model the QWIP current characteristic within a small range of applied bias voltage.

Using the above interpretation, the ideality factor of QWIP-A was extrapolated to be $n = 1.8$. The saturation current, I_s, at $V = 0$ is $1.2 \times 10^{-4} A$. Fig. 2.9 shows the measured dynamic resistance of QWIP-A and r_d calculated from Eq. (2.27). The dark current calculated from Eq. (2.26) is plotted in Fig.2.10 using the above extracted parameters. Comparing the measured and modelled current, this current expression models the dark current well up to 0.02 V.

The same strategy was applied to QWIP-B and we got $n = 3.1$ and $I_s = 1.8 \times 10^{-7} A$. The measured dynamic resistance of QWIP-B as well as the r_d calculated from Eq. (2.27) are plotted in Fig. 2.11 to show how the parameter was extracted. Based on the extracted parameters, the dark current of QWIP-B was calculated and plotted in Fig. 2.12. Eq. (2.26) models the dark current well up to 0.02 V for QWIP-B.

As we mentioned in section 2.4, the dynamic resistance characteristic of QWIP-C is different from QWIP-A and QWIP-B due to the strain effect. When we apply a voltage to QWIP-C, under low bias condition, the dynamic resistance decreases

when the applied voltage increases. Once the applied voltage overcomes the interface voltage, the conduction behavior becomes similar to QWIP-A and QWIP-B. We extrapolated the ideality factor in the region without the interface voltage effect, at $V = 17mV$, and found $n = 5.9$, $I_s = 8.5 \times 10^{-6} A$. Fig. 2.13 shows the measured dynamic resistance as well as the r_d calculated from Eq. (2.27) for extraction. The dark current calculated from Eq. (2.26) was plotted in Fig. 2.14 using the extracted values for n and I_s. Since V_{bi} of QWIP-C is about 17 mV, the current model will not describe the current well for $V < 0.017$ V. Obviously, Eq. (2.26) does not describe the dark current characteristic well for QWIP-C.

Table 2.1: Device parameters for the measured QWIPs.

QWIP	A	B	C
SL barrier	$In_{0.52}Al_{0.48}As$	$Al_{0.32}Ga_{0.68}As$	$Al_{0.4}Ga_{0.6}As$
m^*	$0.0736m_0$	$0.0849m_0$	$0.0895m_0$
ϵ_r	12.7	11.9	11.7
Width (Å)	35	78	30
SL well	$In_{0.53}Ga_{0.47}As$	GaAs	GaAs
Width (Å)	50	26	59
L_b (Å)	460	598	475
QW	$In_{0.53}Ga_{0.47}As$	GaAs	$In_{0.07}Ga_{0.93}As$
m^*	$0.0456m_0$	$0.0665m_0$	$0.0637m_0$
ϵ_r	13.5	12.1	12.4
Width (Å)	110	85	106
$N_D(10^{18}cm^{-3})$	0.5	0.4	1.4
Periods	20	30	20
Substrate	InP	GaAs	GaAs
Mesa (μm^2)	1.92×10^5	4×10^4	4.9×10^4
Transition	BTM	BTM	SBTM

BTM : Bound-to-miniband transition.

SBTM : Stepbound-to-miniband transition.

Table 2.2: Energy level[1] and related parameters for the measured QWIPs.

QWIP	A	B	C
ΔE_c (meV)	500	260	388
Step (meV)	0	0	66
E_{BS} (meV)	35	32	22
E_{MB} (meV)	160–192	165–171	136–153
E_f(no dopant overshoot) (meV)	38	31	28
W (Å)	106	25	—
ϕ (mV)	38	2	—
E_f(with dopant overshoot)[2] (meV)	63	35	—

1 : Energy levels are reference to the bottom of conduction band edge.
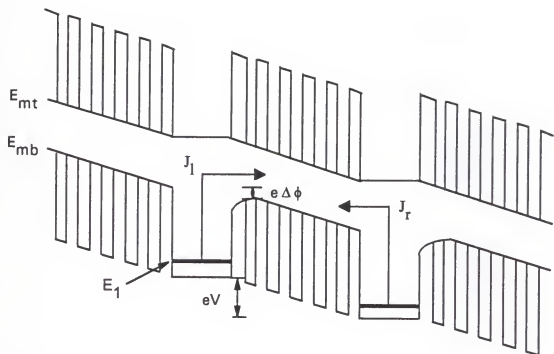
2 : $E_{BS} - E_D \approx 1\text{meV}$

Figure 2.1 Band diagram of a BTM QWIP with an applied reverse bias voltage V per period.
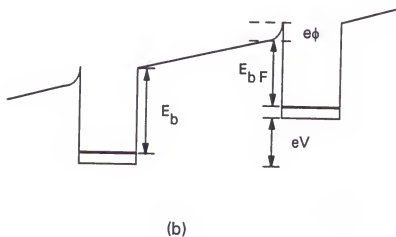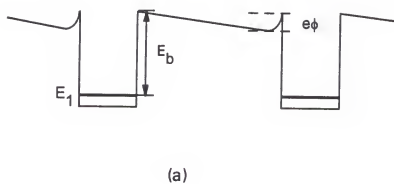
(a)

(b)

Figure 2.2 (a) Energy band structure of a QWIP without external field.
(b) Energy band structure with an applied forward bias.

Figure 2.3 Forward bias dark current versus applied voltage per period for QWIP-A.

Figure 2.4 Reverse bias dark current versus applied bias voltage per period for QWIP-A.
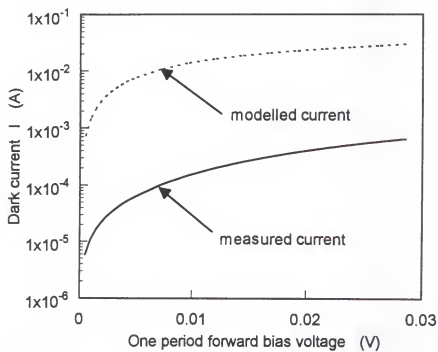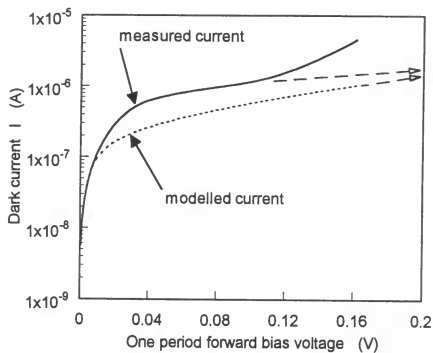
Figure 2.5 Forward bias dark current versus applied bias voltage per period for QWIP-B.
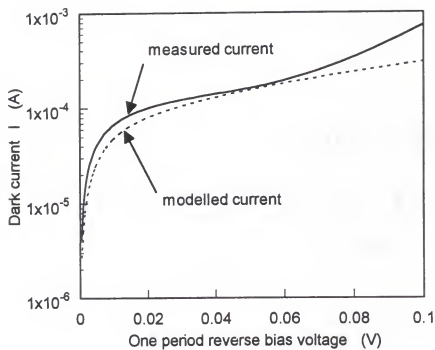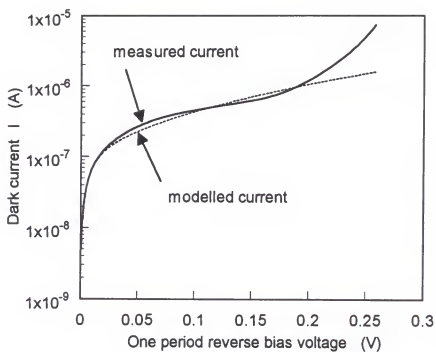
Figure 2.6 Reverse bias dark current versus applied bias voltage per period for QWIP-B.
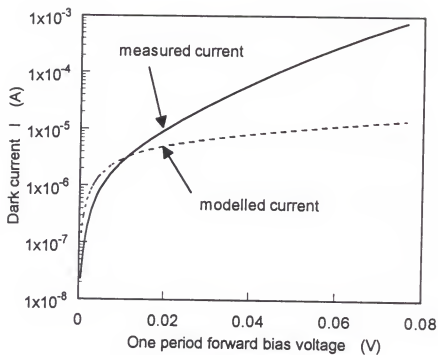
Figure 2.7 Forward bias dark current versus applied bias voltage per period for QWIP-C.
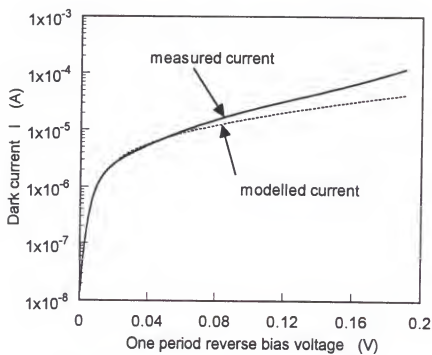
Figure 2.8 Reverse bias dark current versus reverse applied voltage per period for QWIP-C.

Figure 2.9 Dynamic resistance versus reverse bias voltage per period for QWIP-A.

Figure 2.10 Dark current versus reverse bias voltage per period for QWIP-A.
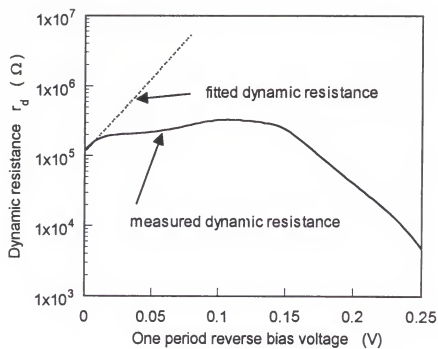
Figure 2.11 Dynamic resistance versus reverse bias voltage per period for QWIP-B.
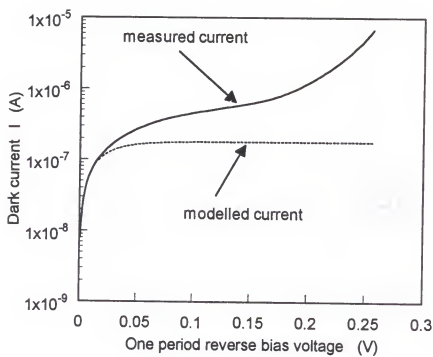
Figure 2.12 Dark current versus reverse bias voltage per period
for QWIP-B.
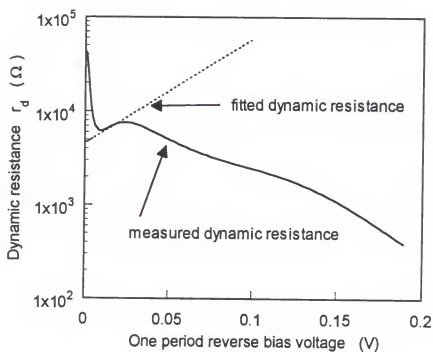
Figure 2.13 Dynamic resistance versus reverse bias voltage per period for QWIP-C.
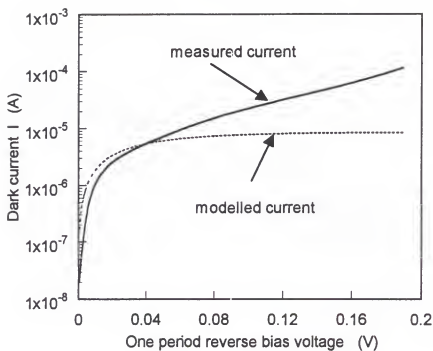
Figure 2.14 Dark current versus reverse bias voltage per period
for QWIP-C.

CHAPTER 3
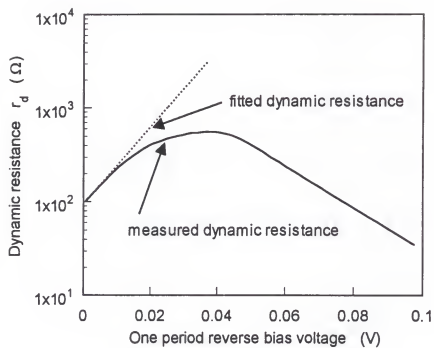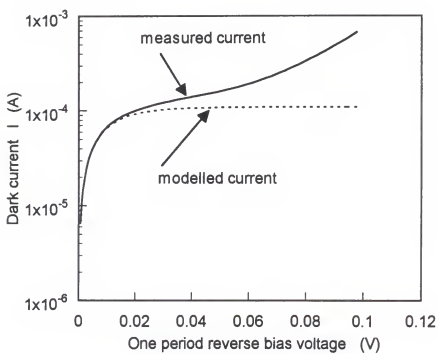## CURRENT CONDUCTION UNDER LOW BIAS OPERATION

3.1 <u>Introduction</u>

In a homogeneous photoconductor, the generation-recombination (g-r) noise current spectral density is related to the dark current, I_D, through[37]

$$S_i = 4qI_Dg \tag{3.1}$$

where q is the charge of the conducting carrier and g is defined as the noise gain. This formula has been widely used to interpret QWIP noise behavior[38]–[42]. Implicitly, the relation between the noise characteristics and the charge transport mechanism is phenomenologically expressed by the noise gain.

In stead of using the phenomenological noise gain to relate the dark current and noise current, a current model based on a concept inferred from the QWIP noise characteristics with the additional assumption that the charge transport process is emission limited is derived to describe the current-voltage characteristics under a low electric field condition. This current model was examined for both bound-to-continuum transition (BTC) and bound-to-minband transition (BTM) QWIPs. The excellent agreement between the measured and calculated dark currents confirms our model assumptions.

3.2 Device Operation under Equilibrium

Detailed noise measurements on both n-type and p-type QWIPs will be presented in chapter 4 and chapter 5. Under low electric fields[33], the results showed that the thermally generated conducting carriers diffuse, on the average, to the nearest neighboring quantum well where they subsequently recombine. From this observation, the following picture emerges for the operation of a QWIP at zero bias: Carriers are being thermally generated from the quantum well bound states into the extended continuous states with, in equilibrium, equal probabilities for transferring to the next neighboring quantum well on the anode or cathode side. The carrier lifetime in the bound states τ_s can be calculated from[33]

$$\overline{G} = P_s/\tau_s \tag{3.2}$$

where $\overline{G}$ is the equilibrium thermal generation rate and P_s is the number of carriers in the bound states.

The thermal generation rate per unit volume of the n-type miniband QWIPs discussed in chapter 2 is around $10^{23} cm^{-3} s^{-1}$ at 77K resulting in the electron lifetime to be about 5 μs[32]. The thermal generation rate of QWIP-D is $3.8 \times 10^{22} cm^{-3} s^{-1}$ at 100K resulting in a hole lifetime of 53 μs [33]. The above two examples show that, in general, the τ_s value is large compared to the intra-well carrier scattering time which we estimate in the picosecond range thus, allowing the carriers to fully thermalize in the wells. This thermalization process decouples the statistical fluctuations in carrier transport through a barrier region from one section to the next.

As a result, if the ratio of the active device length over the extended state carrier trajectory is equal to M, a QWIP can be thought of as consisting of M, statistically independent, sections each made up of a barrier region with two doped quantum wells as contacts from which the carriers are emitted.

3.3 Thermal Generation Current

In equilibrium, the net current through any cross-sectional plane is zero which results from the detailed balance between two opposing thermally generated currents I_0. Assuming full shot noise in each current, the current noise spectral density of a single section is[30]

$$S_{i(section)} = 4qI_0 \tag{3.3}$$

where q is the charge of the carrier. The measured current noise from M statistically independent sections in series becomes then

$$S_i = \frac{S_{i(section)}}{M} \tag{3.4}$$

Using the Nyquist expression, the current noise spectral density is calculated as

$$S_{i(Nyquist)} = \frac{4kT}{R_{(ac)}} \tag{3.5}$$

where k is the Boltzmann constant, T is the temperature in Kelvin, and $R_{(ac)}$ is the dynamic resistance of the device in equilibrium. From Eq. (3.3), (3.4), and (3.5), the generation current I_0 is derived to be

$$I_0 = \frac{MkT}{qR_{(ac)}} \tag{3.6}$$

Since the dynamic resistance can be calculated by differentiating the dark current with respect to applied voltage, the thermally generated dark current in equilibrium can be obtained if the value of M is known.

3.4 Dark Current Model under Low Fields

Without applying bias voltage to the device, the activation energy seen by the carriers in the quantum well ground states is E_b. The thermal generation current I_0 is proportional to $\exp(-E_b/kT)$. When an electric field is present, the energy band diagram will be tilted and the effective energy barrier will be reduced by approximately $\Delta E_{\mathcal{E}} = q\mathcal{E}_w L_w$, where $\mathcal{E}_w$ is the electric field in the well and L_w is the well

width. This barrier lowering effect due to the electric field will cause an increase in the carrier generation rate resulting in an increase in the thermal generation current value. In addition, image-force-induced barrier lowering should be taken into account because of the high doping concentration in the quantum wells.

Using the Schottky model, the barrier lowering $q\Delta\phi$ is given by[34]

$$q\Delta\phi = q\sqrt{\frac{q\mathcal{E}_b}{4\pi\epsilon_r\epsilon_0}} \qquad (3.7)$$

where $\mathcal{E}_b$ is the applied field present in the barrier region, ϵ_r is the dielectric constant, and ϵ_0 is the free space permittivity. The total energy barrier lowering ΔE, including both the electric field effect and the Schottky image effect, can be expressed as

$$\Delta E = q\Delta\phi + q\mathcal{E}_w L_w \qquad (3.8)$$

Hence, the thermal generation current with a bias voltage applied becomes

$$I_{th} = I_0 \exp(\frac{\Delta E}{kT}) \qquad (3.9)$$

where we assume that the charge transport process is emission limited and not collision limited. When an electric field is present producing a voltage drop V_b across a section, the total net current emitted from two opposing quantum wells is given by

$$I = I_{th}[1 - \exp(-\frac{qV_b}{kT})] \qquad (3.10)$$

In equilibrium, the saturation current I_{th} is equal to I_0 and the total current will become equal to zero.

3.5 Measured and Modelled Dark Currents

Dark currents of two p-type BTC transition QWIPs are presented in section 3.5.1 and compared to the current model. Section 3.5.2 compares the measured dark current with modelled current for three BTM QWIPs including two n-type QWIPs

discussed in the previous chapter. Table 3.1 lists the device parameters of three p-type QWIPs used in this study, where λ_p is the spectral response peak in wavelength, L_b is the width of the barrier, and N is the number of periods.

3.5.1 Dark current for BTC QWIPs

The I_0-values of QWIP-D were calculated from Eq. (3.6) for different temperatures using M=N. Table 3.2 shows these I_0-values and the relevant parameters.

Assuming a position independent electric field under low bias voltage, the dark current-voltage characteristic of QWIP-D was calculated using the extracted I_0-values and compared with measured data in Fig. 3.1 for different temperatures. The good agreement between the calculated and measured dark current supports our model that at low fields the holes are thermally generated from a quantum well and travel, on average, one period before they trap into the nearest neighboring quantum wells, i.e., M=N. When the applied field becomes higher a significant fraction of the holes will travel more than one period, revoking the assumption of M statistically independent sections. Consequently, Eq. (3.10) can no longer be used to calculate the current characteristic of the QWIP.

Fig. 3.2 shows the dark current-voltage characteristics of QWIP-E. Again, the current was calculated assuming a constant applied electric field throughout the device and M=N. A good agreement between the calculated and measured data indicates that again, as in QWIP-E the holes travel one period before they recombine. The pertinent parameters for QWIP-E are listed in Table 3.3.

3.5.2 Dark current for BTM QWIPs

Fig. 3.3 shows the measured dark current as well as the modelled current for QWIP-F which is a stepbound-to-miniband p-type QWIP. In the current calculation, M is assumed equal to N. To obtain good agreement between the measured and

modelled current values, we assumed that the electric field inside the quantum well is only 67% of the value in the barrier region. This seems to be a reasonable assumption if one takes into account that the quantum wells in this device have a higher doping density than the wells in the other QWIPs. Our current model predicts correctly the current for all temperatures and bias voltages measured indicating that holes travel one period before recombining into the quantum wells in this miniband QWIP. Table 3.4 lists the pertinent parameters for calculating the QWIP-F dark current.

Fig. 3.4 shows the dark current for two n-type miniband QWIPs at 77K. The dynamic resistance for QWIP-B is 4.3 MΩ resulting in a value for the current spectral density of $1 \times 10^{-27} A^2/Hz$. Due to the small effective mass of an electron in GaAs, the carrier mobility and thus the conductivity in a n-type QWIP quantum well is much higher than in a p-type QWIP quantum well. Therefore, using current continuity we may argue that the voltage drop inside the n-type wells can be neglected. By treating this n-type QWIP as N statistically independent sections in series, we found good agreement between the calculated dark current and the measured data up to 5V, indicating that on the average the electrons travel one period before recombining.

The dynamic resistance of QWIP-A is 2 KΩ which results in a current spectral density value of $2 \times 10^{-24} A^2/Hz$. Instead of assuming N statistically independent sections in series for this QWIP, we used $M = \frac{N}{2}$ in our dark current calculation to obtain agreement between theory and experiment up to 1.5V, indicating that electrons travel two periods before they recombine into quantum well ground states in this bias range.

In summary, we have proposed and verified a model for low bias device operation of n- and p-type QWIPs. The QWIPs can be thought of as consisting of M statistically independent sections, where M is equal to the ratio of the device length over the average traveling distance of the mobile carriers under low fields.

Table 3.1: Device parameters for three different p-type QWIPs.

D.U.T.	BTC QWIP		SBTM QWIP
	QWIP-D	QWIP-E	QWIP-F
QW	$In_{0.2}Ga_{0.8}As$	$In_{0.15}Ga_{0.85}As$	$In_{0.12}Ga_{0.88}As$
L_w (Å)	48	48	90
barrier	$Al_{0.15}Ga_{0.85}As$	$Al_{0.1}Ga_{0.9}As$	$GaAs/Al_{0.35}Ga_{0.65}As$
L_b (Å)	500	500	490
λ_p (μm)	7.5	9.2	10
doping (cm^{-3})	2×10^{18}	2×10^{18}	3×10^{18}
N	20	20	20
area (m^2)	4.7×10^{-8}	7.5×10^{-8}	4.7×10^{-8}
M	N	N	N

Table 3.2: I_0-values and related parameters for QWIP-D.

T (K)	$R_{(ac)}$ (Ω)	$S_{i(Nyquist)}$ (A^2/Hz)	I_0 (A)
80	16.8 M	2.6×10^{-28}	8.1×10^{-9}
89	1.65 M	3.0×10^{-27}	9.4×10^{-8}
100	145 K	3.8×10^{-26}	1.2×10^{-6}
112	21.6 K	2.9×10^{-25}	9.1×10^{-6}
130	2.25 K	3.2×10^{-24}	1.0×10^{-4}

Table 3.3: I_0-values and related parameters for QWIP-E.

T (K)	$R_{(ac)}$ (Ω)	$S_{i(Nyquist)}$ (A^2/Hz)	I_0 (A)
42	6.0 M	3.9×10^{-28}	1.2×10^{-8}
50	3.1 M	8.9×10^{-28}	2.8×10^{-8}
60	1.0 M	3.3×10^{-27}	1.0×10^{-7}
70	140 K	2.8×10^{-26}	8.8×10^{-7}
77	28 K	1.5×10^{-25}	4.7×10^{-6}

Table 3.4: I_0-values and related parameters for QWIP-F.

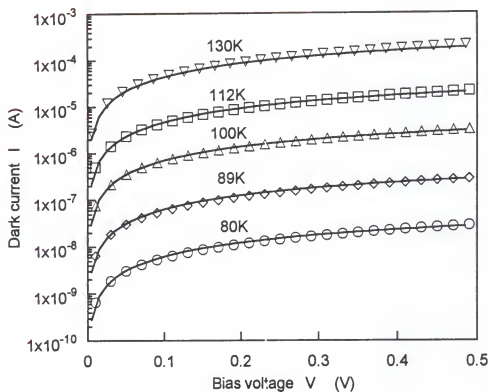| T (K)	$R_{(ac)}$ (Ω)	$S_{i(Nyquist)}$ (A^2/Hz)	I_0 (A)
49	27 M	1.0×10^{-28}	3.1×10^{-9}
61	710 K	4.7×10^{-27}	1.5×10^{-7}
71	69 K	5.7×10^{-26}	1.8×10^{-6}
77	21 K	2.0×10^{-25}	6.3×10^{-6}
87	4.9 K	9.8×10^{-25}	3.1×10^{-5}

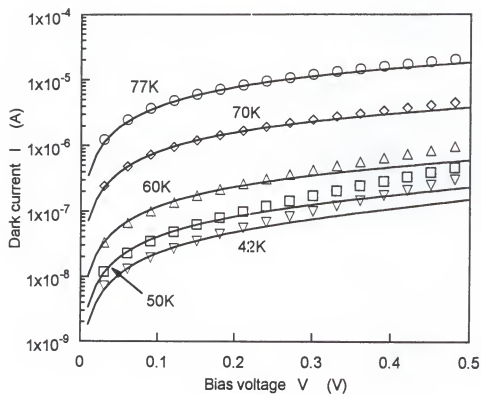**Figure 3.1** Dark current versus bias voltage for QWIP-D.

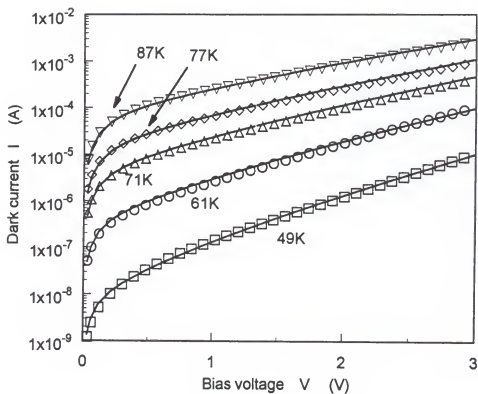**Figure 3.2** Dark current versus bias voltage for QWIP-E.

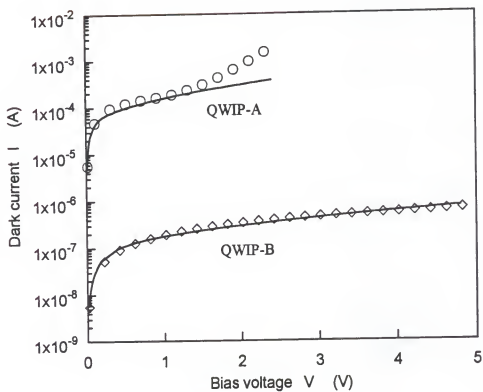**Figure 3.3** Dark current versus bias voltage for QWIP-F.

Figure 3.4 Dark current versus bias voltage for QWIP-A and QWIP-B at 77K.

CHAPTER 4
NOISE CHARACTERIZATION OF N-TYPE BOUND-TO-MINIBAND TRANSITION QWIPS

4.1 Introduction

Dark current noise measurements between 10^1 and 10^5 Hz were carried out at 77K on three different III-V quantum well infrared photodetectors (QWIPs) designed for 8-12μm infrared (IR) detection[32]. These devices have superlattice (SL) barriers leading to miniband transport in the extended conduction band. Two of the QWIPs are bound-to-miniband (BTM) transition QWIPs[6]. The other QWIP is a step-bound-to-miniband (SBTM) transition QWIP[4]. Two types of noise contributing to the overall spectrum were identified. At low and moderate applied voltage values, generation-recombination (g-r) noise is the dominant noise source. This type of noise is due to fluctuations in the trapping and detrapping rates of electrons in the quantum well boundstates. At zero bias, the current noise spectral density of the g-r noise conforms to the well-known Nyquist expression as predicted by Rose[37]. At high bias voltage, $1/f$-like noise becomes large and dominant. The noise measurements provide not only the output noise current used in detectivity calculations but also an alternate method to determine the gain of a QWIP.

4.2   Device Description

4.2.1   Physical structure

Device parameters are listed in Table 2.1, where, L_b represents the total superlattice (SL) barrier width between two adjacent, photonic active, quantum wells (QW), and N_D denotes the donor doping concentration of the quantum wells.

QWIP-A was grown on a semi-insulating InP substrate. A 1-μm $In_{0.53}Ga_{0.47}As$ buffer layer with doping density of $2 \times 10^{18} cm^{-3}$ was first grown on the InP substrate, followed by the growth of 20 periods of $In_{0.53}Ga_{0.47}As$ quantum wells with a well width of 110Å and a dopant density of $5 \times 10^{17} cm^{-3}$. The layers on each side of the quantum well consist of 6 periods of undoped $In_{0.52}Al_{0.48}As$ (35Å) / $In_{0.53}Ga_{0.47}As$ (50Å) superlattice barrier layers. A 0.3-μm n^+-$In_{0.53}Ga_{0.47}As$ cap layer with a dopant density of $2 \times 10^{18} cm^{-3}$ was grown on top. The mesa structure for the QWIP was formed by chemical etching through the QWIP active layers and stopped at the n^+-$In_{0.53}Ga_{0.47}As$ buffer layer for ohmic contact. The ohmic contact was formed by using electron beam (E-beam) evaporation of AuGe/Ni/Au films. The top area of the mesa is $1.92 \times 10^5 \mu m^2$.

QWIP-B has the same structure as QWIP-A but uses different materials and parameters. The buffer layer (1 μm) of QWIP B is GaAs with a dopant density of $1.4 \times 10^{18} cm^{-3}$. Thirty periods containing a GaAs quantum wells with a well width of 85Å and doping concentration of $4 \times 10^{17} cm^{-3}$ were used. The barrier layers are formed by 6 periods of undoped GaAs (26Å) / $Al_{0.32}Ga_{0.68}As$ (78Å) superlattice layers. The cap layer was formed by a 0.3-μm GaAs layer with a doping concentration of $2 \times 10^{18} cm^{-3}$. The top area of this QWIP is $4 \times 10^4 \mu m^2$.

The buffer and cap layers of QWIP-C consist of GaAs with a doping concentration of $1.4 \times 10^{18} cm^{-3}$. The thicknesses of these two layers are 1 μm and 0.4 μm, respectively. Twenty periods containing an $In_{0.07}Ga_{0.93}As$ quantum well with a

well width of 106Å were used in this QWIP. The materials used for the superlattice barriers are GaAs (59Å) / $Al_{0.4}Ga_{0.6}As$ (30Å). The top area of the etched mesa is $4.9 \times 10^4 \mu m^2$.

4.2.2 Energy band diagram

The parameters of the energy band diagrams are listed in Table 2.2. The symbol ΔE_c represents the conduction band offset in the quantum wells. E_{BS} and E_{MB} stand for the bound state energy level and the miniband energy position, respectively, which are referenced with respect to the bottom of the conduction band edge.

The conduction-band discontinuity for QWIP-A is taken as $\Delta E_c = 500$ meV. The ground state of the quantum well lies 35 meV above the conduction-band edge. The miniband minimum is located at 160 meV and the width of this miniband is about 32 meV.

QWIP-B has a conduction-band discontinuity $\Delta E_c = 260$ meV. The ground state is at 32 meV and the miniband starts at 165 meV with a width of 6 meV.

For QWIP-C, $\Delta E_c = 388$ meV, the ground state of the quantum well is $E_{BS} = 22$ meV, and the miniband ranges from 136 meV to 153 meV above the bottom of the quantum well.

The values of bound state and miniband energy levels were calculated using a numerical method introduced by Shenoy[43]. For the bound state calculation, the electron-electron interaction was also taken into account[44]–[45].

4.3 Measurement Setup

We performed four measurements in order to distinguish the low noise spectral density of the QWIPs from the amplifier noise contribution[46]. The schematic diagram of the first noise measurement is shown in Fig. 4.1. Each front-end element

of the measuring setup has corresponding noise sources associated with it as depicted in Fig. 4.2.

The Low Noise Amplifier (LNA) is modelled as a noise-free amplifier with gain G and an input resistance R_i and two input noise sources S_{ia}, S_{va} as indicated in Fig. 4.2. The metal thin film resistors used in the bias networks are represented as noise-free resistors in parallel with a current noise source of current spectral density $S_R = \frac{4k_BT}{R}$. The QWIP is modelled as a current noise source of spectral density S_{id} in parallel with its dynamic resistance r_d. The wet-cell battery used to bias our devices is assumed to act as a short for a.c. signals due to its very high capacitance. With this model, the reading of the spectrum analyzer, $M_1{}^2$, equals

$$M_1{}^2 = G^2 \left[S_{va} + (S_{ia} + S_{ibias} + S_{id})\overline{R}^2 \right] \tag{4.1}$$

where,

$$\overline{R} = \frac{R_i \cdot R_{bias} \cdot r_d}{(R_i R_{bias} + R_i r_d + R_{bias} r_d)}, \text{ the resistance of } R_i, R_{bias}, \text{ and } r_d \text{ in parallel.}$$

$$R_{bias} = \frac{R_a \cdot R_b}{(R_a + R_b)} + R_c, \text{ the a.c. equivalent resistance of the bias resistors,}$$
$$R_a, R_b, \text{ and } R_c.$$

$$S_{ibias} = \frac{4k_BT}{R_{bias}}, \text{ the overall noise current generated by the bias resistors.}$$

In the second measurement, we replaced the QWIP by a metal thin film resistor, R_d, of the same value as the dynamic resistance of the QWIP. The second reading of the spectrum analyzer becomes

$$M_2{}^2 = G^2 \left[S_{va} + (S_{ia} + S_{ibias} + S_{iRd})\overline{R}^2 \right] \tag{4.2}$$

where, $\overline{R}$ in Eq. (4.2) is equal to $\overline{R}$ in Eq. (4.1) and S_{iRd} equals $\frac{4k_BT}{r_d}$.

For the third measurement, we added a noise source which is built internally in the HP3561A analyzer, in series with R_d. The internal resistance of the noise source is 50 Ω and its noise is modeled as a voltage source with a spectral density S_{Vcal} in

series with a 50 Ω resistor. For the QWIPs under study, the dynamic resistance is generally much larger than the internal resistance of the noise source. We can then simplify the a.c. equivalent circuit of our third measurement and the third reading becomes

$$M_3{}^2 = G^2 \left[S_{va} + \left(S_{ia} + S_{ibias} + S_{iRd} + \frac{S_{Vcal}}{r_d{}^2} \right) \overline{R}^2 \right] \tag{4.3}$$

The last measurement consists of measuring the value S_{Vcal} by connecting the noise source directly to the HP3561A spectrum analyzer. From this measurement $M_4{}^2$ is given by

$$M_4{}^2 = S_{Vcal} \tag{4.4}$$

With a simple algebraic manipulation of Eq. (4.1) through Eq. (4.4), we obtain

$$S_{id} = \left(\frac{M_1{}^2 - M_2{}^2}{M_3{}^2 - M_2{}^2} \right) \cdot \frac{M_4{}^2}{r_d{}^2} + \frac{4k_B T}{r_d} \tag{4.5}$$

which is the current spectral density of the QWIP being measured. The HP3561A spectrum analyzer has a bandwidth of 100 kHz and allows data collection via a computer. During the measurements the QWIPs were submerged into liquid nitrogen to maintain a 77K lattice temperature.

4.4 Dark Current and Dynamic Resistance

An important parameter entering in our noise expressions is the dynamic resistance of the QWIP. In order to find this parameter, we measured the dark current of our samples first. Dark current was measured using a HP4145B parameter analyzer and the QWIP device was also submerged into liquid nitrogen during the measurement.

The dynamic resistance is calculated by using the first term of a Newton-Gregory central polynomial approximation[47],

$$f'(x) = \frac{f(x+h) - f(x-h)}{2h} \tag{4.6}$$

The interpolating interval constant h for QWIP-B was chosen to be 0.02V. For QWIP-A and QWIP-C, the constant h was 0.01V. Fig. 4.3, Fig. 4.4, and Fig. 4.5 show the dark current as well as the dynamic resistance versus bias voltage for these three QWIPs at 77K. The asymmetry of the current-voltage characteristic is due to growth artefacts[22] and has been discussed in chapter 2.

4.5   Experimental Results and Discussion

In all the n-type QWIP applications, the device is always operated in the reverse bias regime which has a lower dark current resulting in a better detectivity. Therefore, our QWIP noise characteristic studies mainly focus on this regime of operation.

4.5.1   Current noise spectral density

Typical current noise spectra of QWIP-A are shown in Fig. 4.6 for four different bias voltages. In the intermediate frequency range ($f > 1KHz$), the noise spectral density is affected by RC parasitic effects, but after corrections are made, frequency independent noise levels result. These noise plateaus are attributed to electron trapping and detrapping in the quantum well bound states. At lower frequencies, the spectral density was large and presumably due to external effects such as pick up or boiling of the nitrogen or due to internal mechanisms such as electron trapping in defects. When the reverse bias voltage was greater than $-1.06V$ and forward bias voltage greater than $0.104V$, the $1/f$ noise became so large that it dominated the g-r noise.

Although the transition mechanism of QWIP-B and QWIP-A is identical, the material used to form the quantum wells of QWIP-B is GaAs in stead of InGaAs. The heavier effective mass of GaAs over InGaAs gives a higher density of states in the quantum wells. Therefore, even though QWIP-B has a similar doping concentration as QWIP-A, the dark current is much lower resulting in the d.c. resistance as well as

the dynamic resistance for this QWIP to be extremely high. Because of the relatively high dynamic resistance, especially at low applied bias voltage, low bias device noise values fall below the detection limit of our setup. We measured the current noise spectral density under relative high bias voltages and the typical spectra are shown in Fig. 4.7. Due to electric break down of the device, the highest reverse bias voltage reached was -7.4V. The strong signal at low frequencies is attributed to the same mechanisms as in QWIP-A. Neglecting this signal in the spectrum, the noise level S_i is independent of frequency.

The material chosen for the quantum wells of QWIP-C has a lower conduction band edge than the material used in the superlattice barriers. As a result, the ground state inside the quantum well has a lower energy level than the conduction band edge of the superlattice barriers. The purpose of this design is to lower the dark current of the device[4]. Noise measurements were performed on this QWIP for forward bias voltages between $0.255V$ and $1.19V$, and reverse bias voltages between $-0.267V$ and $-3.88V$. We found that QWIP-C displays quantum well g-r noise up to a forward bias of $0.9V$ and a reverse bias of $-3.1V$ after which $1/f$ noise again becomes dominant. Typical current noise density spectra of QWIP-C are shown in Fig. 4.8.

4.5.2 Electron diffusion length and noise gain

The noise measured at intermediate frequencies reveals noise plateau levels which we attribute to electron trapping and detrapping in quantum well boundstates. These noise plateaus are plotted as a function of applied bias voltage in Fig. 4.9. The arrows indicate current noise levels calculated using the Nyquist expression[48]

$$S_i = 4kT\frac{dI}{dV} \qquad (4.7)$$

where k is the Boltzmann constant and T is the temperature of the QWIP in Kelvin.

Rose[37] predicted that there is a critical field $\mathcal{E}_c$ or voltage V_c where, in his own words, the photoconductor noise current exceeds the Johnson or Nyquist value and

becomes field dependent. This view is consistent with the measured data of QWIP-A as shown in Fig. 4.9. In this interpretation, the low field noise is not caused by velocity fluctuations but by the same number fluctuation mechanism which is responsible for the high field or high bias noise levels.

The critical field $\mathcal{E}_c$ is given by[37]

$$\mathcal{E}_c = \frac{kT}{qL_D} \tag{4.8}$$

As mentioned in chapter 3, the electrical field inside the quantum wells is negligible compared to the field in the barrier regions. Assuming a position independent electrical field, the critical voltage can be expressed as

$$V_c = \frac{kT}{qL_D} \cdot L \tag{4.9}$$

where $L = (N + 1)L_b$, L_b is the width of the barrier, N is the number of quantum wells, and L_D is the length of the extended state trajectory, which at low bias could be referred to as diffusion length.

From Fig. 4.9, we infer $V_c = 0.08V$ for QWIP-A, resulting in $L_D = 802\text{Å}$, which is close to the spacing of two barriers (920Å). This seems to indicate that, in or near equilibrium, thermally generated carriers on the average diffuse two barrier regions and then recombine into the quantum wells. This result is consistent with the result in chapter 3.

For QWIP-B and QWIP-C accurate values for V_c can not be determined directly from the noise data presented in Fig. 4.9 due to the fact that the QWIP current noise levels lie below our detection limit. However extrapolating from the high bias noise levels to Nyquist values calculated from Eq. (4.7) results in $L_D = 42\text{Å}$ for QWIP-B and $L_D = 432\text{Å}$ for QWIP-C. The small L_D-value of QWIP-B suggests that the thermally generated electrons, at low bias, trap in the same well they were generated from. The L_D value calculated for QWIP-C is close to the interwell spacing indicating

that thermally generated electrons diffuse to the next adjacent well and recombine there.

Hence the following picture emerges. Electrons are thermally generated in the quantum wells, producing locally an excess electron density in the extended miniband conduction states which subsequently spreads out into the superlattice regions. The extended state electron trajectory, L_D, which might be affected by collision and/or tunneling, our noise measurements and interpretation do not discriminate between these two modes of transport, is terminated by trapping in a quantum well. At zero or low electric fields this turns out to be the quantum well electrons originate from (QWIP-B), the next nearest neighboring well (QWIP-C) or the next to nearest neighboring well (QWIP-A). At higher fields the electron trapping probability becomes smaller, as explained in the next section, which increases the extended state electron trajectory, thereby improving the coupling to the external circuit and increasing the noise gain and the current noise level.

The spectral density for g-r noise in photo conductors is usually expressed as

$$S_{i_{(g-r)}} = 4q\overline{I}g \tag{4.10}$$

where, $-q$ is the electron charge, $\overline{I}$ is the mean current, and g is defined as the noise gain, which is identical to the optical gain at high bias and for deep trap centers[31].

In Fig. 4.10, we plotted the noise gain versus bias voltage. For all three devices the noise gain increases with increasing bias voltage.

4.5.3 Electron trapping probability and thermal electron generation rate

The electron trapping probability can be expressed in terms of noise gain[31] as

$$p = \frac{1}{1 + Ng} \tag{4.11}$$

where, p is the electron trapping probability of a single well, N is the total number of quantum wells of the device, and g is the noise gain calculated from Eq. (4.10).

We plotted the trapping probability versus bias voltage in Fig. 4.11. It shows that the electron trapping probability p decreases with increasing bias voltage and that the trapping probability for QWIP-B is relatively high. This agrees with the physical picture that at low bias the electrons in QWIP-B trap in the well they are generated from. For higher bias, the electron escape probability will increase due to field assisted lowering of superlattice barriers resulting in lower trapping probabilities.

The dark current noise can be expressed as[31]

$$S_i = \frac{4i^2}{NgAL_w} \tag{4.12}$$

where S_i is the spectral current density, I is the dark current, N is the number of quantum wells, g is the thermal electron generation rate per unit volume, A is the device area, and L_w is the width of the quantum well.

We plotted the noise current spectral density versus dark current in Fig. 4.12. The solid lines illustrate an I^2 dependency. QWIP-A shows a clear I^2 dependence. For QWIP-B and QWIP-C, the slight deviation of the measured data from an I^2 dependence in the high dark current region is attributed to an increase in the thermal electron generation rate. This effect is highlighted in Fig. 4.13, where we plotted the thermal electron generation rate g, calculated from Eq. (4.12), versus applied bias voltage. The data of QWIP-A indicate that g is independent of bias voltage within the experimental error, whereas in QWIP-B and QWIP-C g increases exponentially with bias voltage because the electric field inside the well regions of these devices tilts the energy band diagram of the photonic active quantum wells in the direction of carrier flow effectively reducing the thermal activation energy required to excite electrons from the bound state to the miniband state[31]. Since the activation energy reduction is proportional to the applied bias voltage and g depends exponentially on the electron activation energy, an exponential variation of g with the applied bias voltage is expected as is confirmed by the data displayed in Fig. 4.13 for QWIP-B and QWIP-C.

4.6 <u>Conclusions</u>

In this chapter, noise studies on three n-type miniband transition QWIPs have been carried out at 77K. For frequencies between 10^2 and 10^4 Hz, noise plateau levels stemming from the trapping and detrapping of electrons in the quantum wells were observed in QWIPs with superlattice barriers. From the measured noise data, the low bias diffusion length, the bias dependent noise gain, and the electron trapping probability were calculated.

Values for the electron diffusion length indicate that electrons at low bias are either trapped in the well they are generated from, the nearest neighboring well, or the next to nearest neighboring well. The dark current noise is shown to be proportional to the current squared if the thermal electron generation rate is independent of bias voltage.
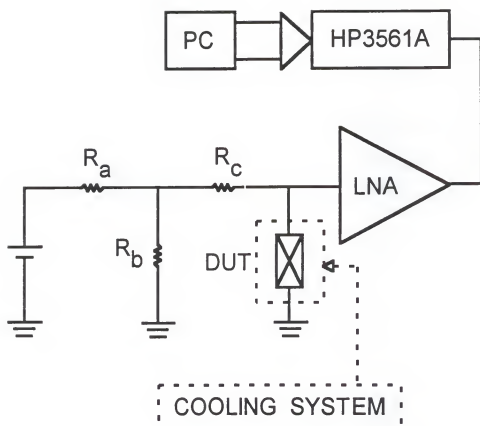
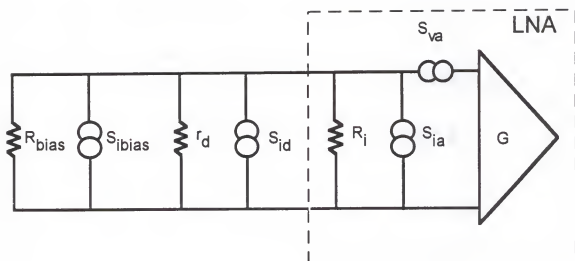**Figure 4.1** Noise measurement setup: the schematic diagram for measuring M_1^2.

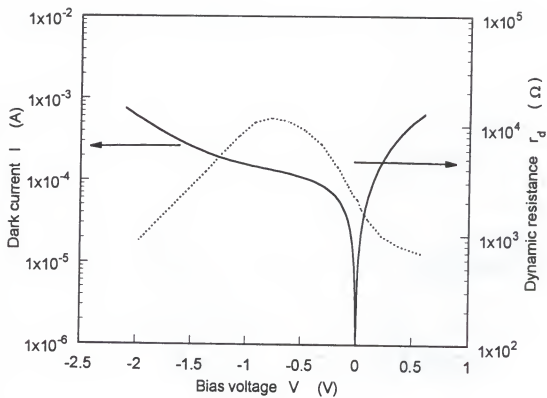**Figure 4.2** Noise measurement setup: noise equivalent circuit for measuring M_1^2.

Figure 4.3 Dark current and dynamic resistance versus applied bias voltage for QWIP-A at 77K.
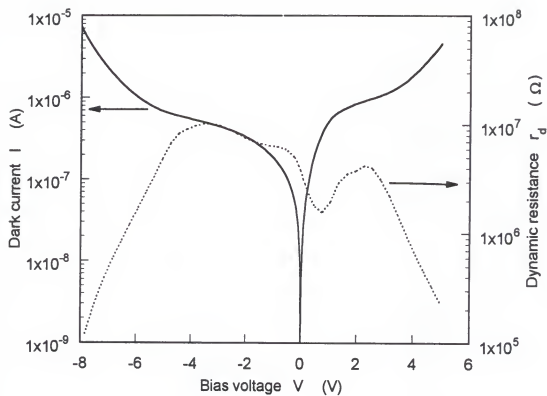
Figure 4.4 Dark current and dynamic resistance versus applied bias voltage for QWIP-B at 77K.
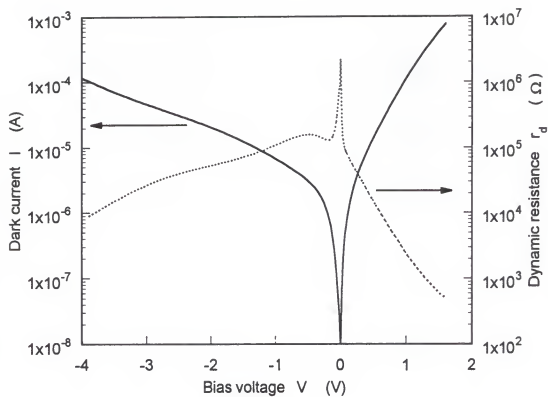
Figure 4.5 Dark current and dynamic resistance versus applied bias voltage for QWIP-C at 77K.
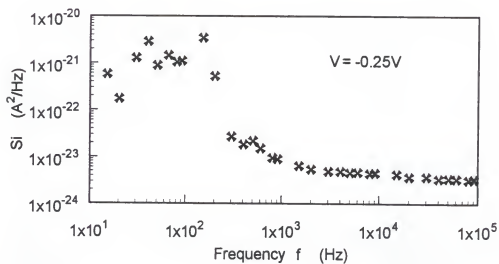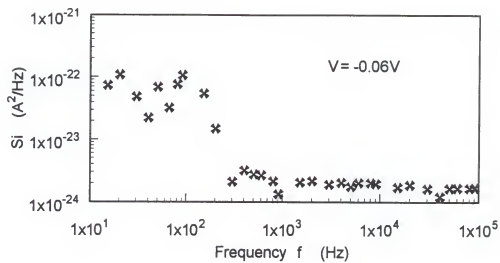
Figure 4.6(a) Current noise spectral density versus frequency for QWIP-A at 77K.

Figure 4.6(b) Current noise spectral density versus frequency for QWIP-A at 77K.

Figure 4.7(a) Current noise spectral density versus frequency
for QWIP-B at 77K.
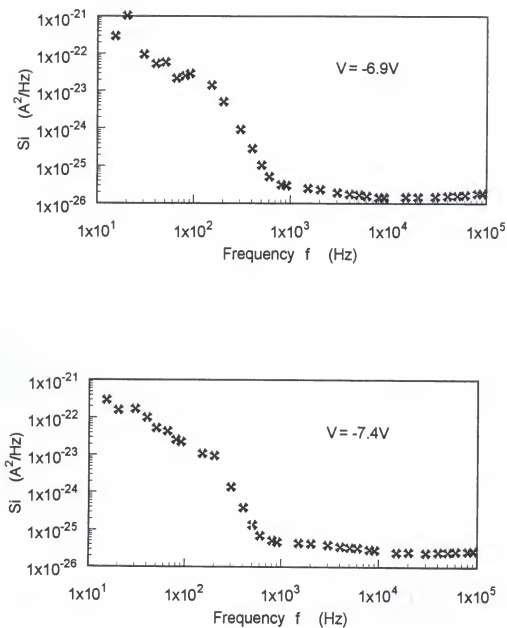
Figure 4.7(b) Current noise spectral density versus frequency for QWIP-B at 77K.
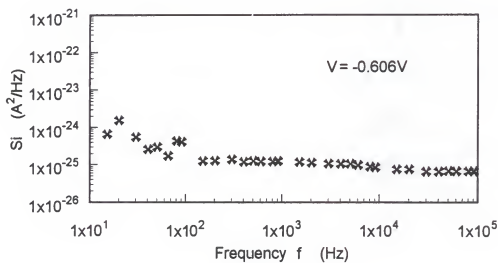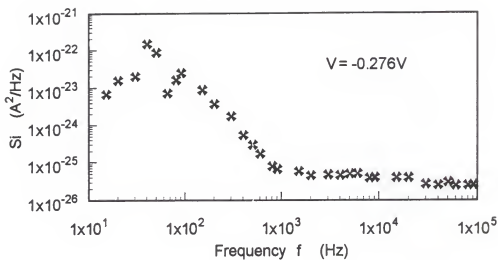
Figure 4.8(a) Current noise spectral density versus frequency
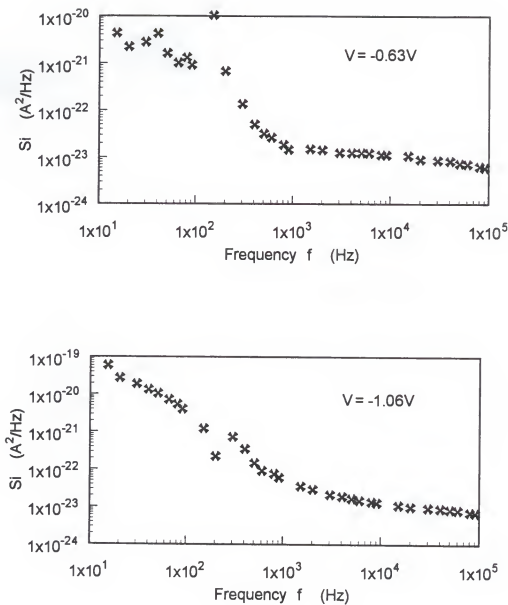for QWIP-C at 77K.
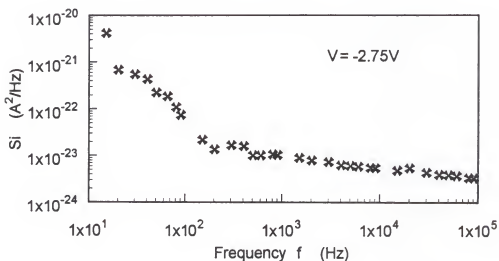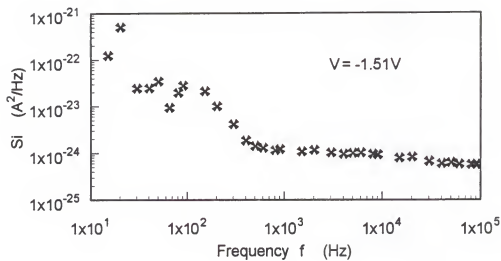
Figure 4.8(b) Current noise spectral density versus frequency
for QWIP-C at 77K.

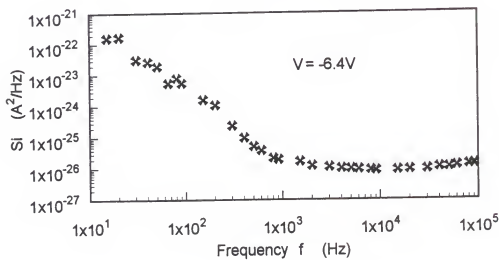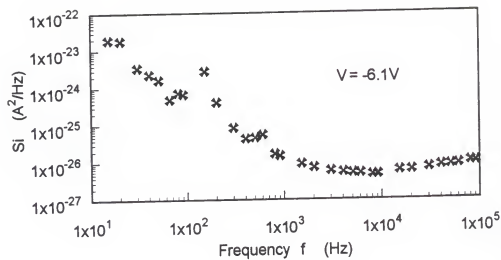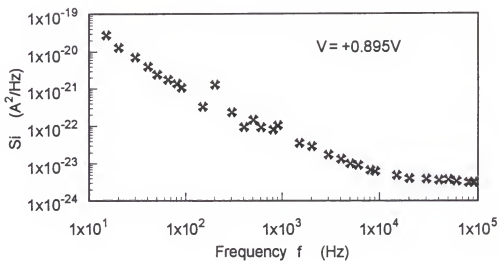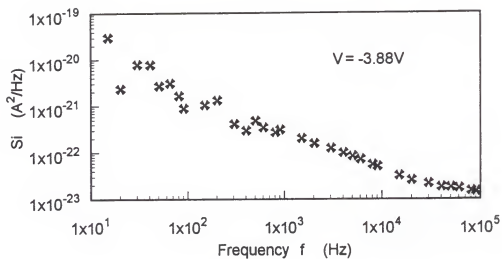Figure 4.8(c) Current noise spectral density versus frequency
for QWIP-C at 77K.
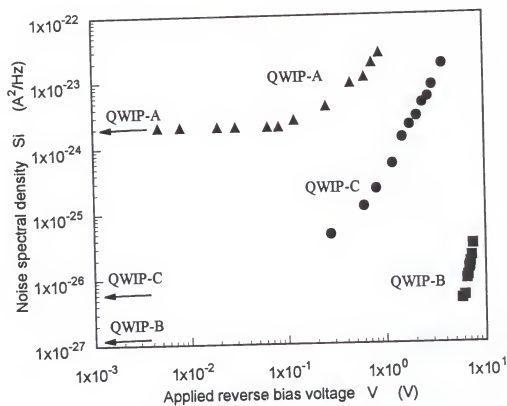
Figure 4.9 Current noise spectral density versus applied reverse bias
voltage at 77K.
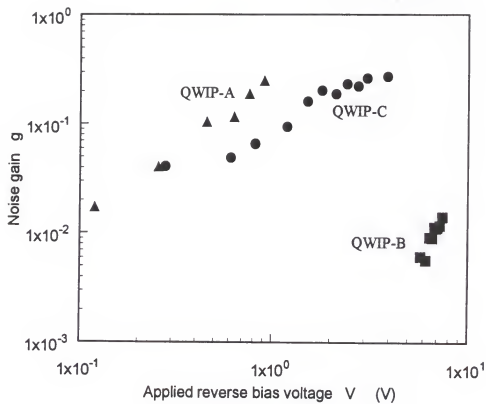
Figure 4.10 Noise gain versus applied reverse bias voltage at 77K.
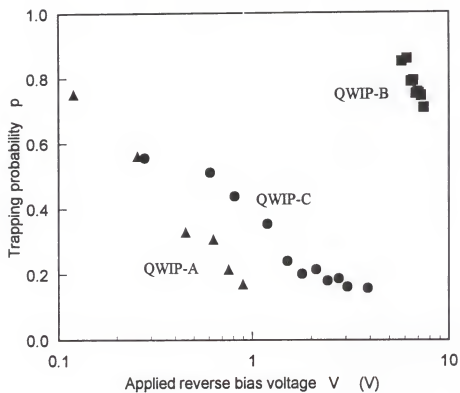
Figure 4.11 Electron trapping probability versus applied reverse bias voltage at 77K.
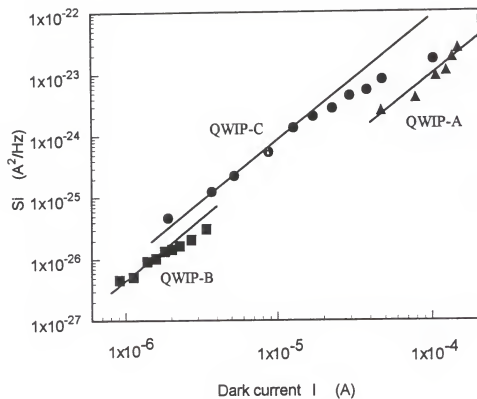
Figure 4.12 Current noise spectral density versus reverse bias dark current at 77K.
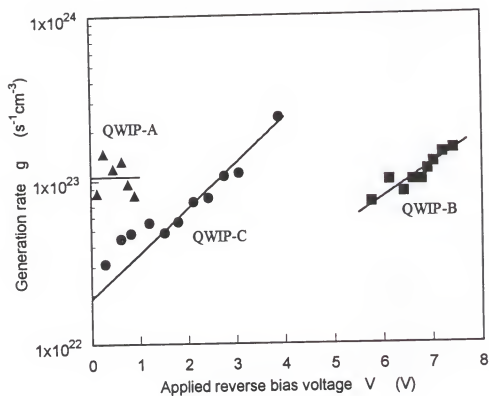
Figure 4.13 Thermal electron generation rate per unit volume versus applied reverse bias voltage at 77K.

CHAPTER 5
NOISE CHARACTERIZATION AND DEVICE PARAMETER EXTRACTION IN P-TYPE STRAINED LAYER QWIPS

5.1 Introduction

In this chapter, the dark current noise measurements between 10^1 and 10^5 Hz were carried out on a compressively strained p-type InGaAs/AlGaAs quantum well infrared photodetector as a function of temperature and bias voltage[33]. The measurement results show that number fluctuation noise associated with the generation and recombination of holes from and to the quantum well bound states and the extended valence band states is the dominant noise source down to 10 Hz. At low bias the number fluctuation noise translates into current fluctuation noise via hole diffusion, whereas at higher bias values the coupling is via the hole drift current component. By applying a wide range of bias voltages, both the diffusion and drift dominant regimes of operation could be investigated. Our measurements indicate that the field induced barrier lowering and the Schottky image effect strongly influence the device characteristics.

In stead of using the generally unknown phenomenological parameters such as noise gain and well capture probability, we developed a model based on a priori known quantities such as the electric field and the quantum well features to explain the observed noise levels in the diffusion and drift regimes. Based upon this model, a value for the low field hole diffusion length and the capture cross-section for hole trapping can be extracted from the noise data. In addition we observe that the

thermally generated heavy holes diffuse, at low fields, on the average to the nearest neighboring quantum well where they subsequently recombine. This recombination process is triggered by hole scattering with the acceptor centers of which the capture cross section could be calculated.

5.2 Device Description

The p-type QWIP under study was grown on a semi-insulating GaAs substrate by molecular beam epitaxy. This QWIP consists of 20 periods of Be-doped $In_{0.2}Ga_{0.8}As$ quantum wells of 48 Å in width with dopant density $2 \times 10^{18} cm^{-3}$, separated by 500 Å undoped $Al_{0.15}Ga_{0.85}As$ barriers. A 0.3 μm cap layer and a 1.0 μm buffer layer of Be-doped AlGaAs with a dopant density of $5 \times 10^{18} cm^{-3}$ were also grown to serve as top and bottom ohmic contacts. The $In_{0.2}Ga_{0.8}As$ quantum wells are in biaxial compression with a designed lattice mismatch of nearly -1.4%. A 100 Å undoped barrier layer of $Al_{0.15}Ga_{0.85}As$ was grown between the contact layer and the QWIP structure to reduce the dark current tunneling through the contact.

The hole transition was designed to be from the heavy hole ground state (HH1) to the third heavy hole state (HH3). The HH1 and HH3 are located 24 meV and 190 meV below the quantum well valance band edge, respectively. The experiments were performed on a $216 \times 216 \mu m^2$ mesa formed by wet chemical etching.

5.3 Experimental Setup

Measurements were carried out using standard noise measurement procedures which have been discussed in chapter 4. A Brookdeal 5004 low noise amplifier (LNA) which has an input referred current noise $S_{ia} \approx 4 \times 10^{-27} \frac{A^2}{Hz}$ was used to amplify the signal generated by the device. Due to the low current noise and high dynamic resistance of this p-type QWIP under low bias conditions, our detection was limited by this amplifier current noise component. The spectral density of the output of the

LNA was measured using a HP3561A spectrum analyzer which has a bandwidth of 100 kHz and allows data collection via a computer.

During the measurement, the device was placed in a CT-310 Cryotran which is a liquid helium flow cryostat made by LakeShore Cryotronics. In stead of using liquid helium as the coolant, liquid nitrogen was used with DTC-500SP temperature controller to vary the device temperature from 81K to room temperature. This cryostat also acted as an external noise shield. In order to extract the device parameters, all the measurements were carried out at temperatures higher than the device BLIP temperature of 63K.

5.4   Measurement Results

The dark currents under both forward and reverse bias voltages were measured using a HP4145B semiconductor parameter analyzer and are shown in Fig. 5.1 for different temperatures. Since the QWIP is a two terminal device, the reverse bias is defined as the direction having a smaller dark current when a bias voltage is applied. The dynamic resistance was calculated using Eq. (4.6) and plotted versus bias voltage in Fig. 5.2 for different temperatures.

Current noise spectra were measured for the reverse bias voltages which are designed to bias the device for IR detection. Our temperature range was determined by the lowest temperature that we could achieve with this setup (81K) and on the high side by the maximum DC current (2 mA) that we allowed to flow through the device. The latter limited our temperature to 130K. Noise spectra were measured from 10 Hz to 100 kHz. Fig. 5.3 shows the typical current noise density spectra at 81K. In the high frequency range ($f > 1$KHz), the noise spectral density is affected by RC parasitic effects, but after corrections are made, frequency independent noise levels result. These noise plateaus are attributed to hole trapping and detrapping in the quantum well bound states. Fig. 5.4 to Fig. 5.7 show the current noise density spectra

for temperature from 89K to 130K, respectively. At higher applied bias voltage or higher temperature, the dynamic resistance is smaller which reduces the RC parasitic effects at high frequency range. This effect can be observed in the measured noise spectra. The measured data indicate that most of the current spectra are frequency independent down to 10 Hz. Only at high bias voltage conditions, eg. $|V_{bias}| > 4$V, excess noise shows up in the spectra for frequencies below 100 Hz.

Fig. 5.8 shows the noise plateau values plotted as a function of dark current for three selected temperatures. From this plot, two different regimes of operation can be recognized. In the low field diffusion dominant regime, noise values are nearly independent of DC current. The observed low bias noise values agree with the values calculated form the Nyquist expression at zero applied bias voltage for all the measured temperatures. In the high field, drift dominant regime however, noise values become strongly current dependent. This general behavior is quite similar to what Rose predicted for traditional photo conductive devices[37].

5.5 Generation-Recombination Noise in P-type QWIPs

5.5.1 Noise mechanism

If the hole lifetime in the valence band is τ_0 and in the quantum well bound state is τ_s, then the particle number spectral density is given by[29].

$$S_P(f) = 4\overline{G}\frac{\tau^2}{1 + \omega^2\tau^2} \tag{5.1}$$

where $\tau^{-1} \approx \tau_0^{-1} + \tau_s^{-1}$ and $\overline{G}$ is the average hole generation rate from the quantum well ground states to the valence band extended states. In equilibrium, the average number of holes generated from the quantum well ground states should equal the average number of holes recombining from the valence band extended states. Assuming the

total number of holes in the valence band is P_0 and in the quantum well bound state is P_s, We have

$$\overline{G} = \overline{R} \quad \text{or} \quad \frac{P_s}{\tau_s} = \frac{P_0}{\tau_0} \tag{5.2}$$

At low temperatures, the total number of holes in the valence band extended states is much smaller than the number of holes in the quantum well ground states of our undoped barrier QWIP device. Therefore, τ_0 is much smaller than τ_s resulting in $\tau \approx \tau_0$. This implies that the particle number spectral density at low frequencies becomes

$$S_P \approx 4\overline{G}\tau_0^2 \tag{5.3}$$

In our p-type QWIP with undoped barriers, the number of mobile holes is equal to the total number of holes excited from the quantum well ground states. The dark current, I_d, can be expressed as

$$I_d = qvpA = qv\frac{P_0}{L} \tag{5.4}$$

where v is the average hole velocity, p is the hole density in the valence band, A is the device cross-sectional area, and L is the active device length. Then, the noise current spectral density can be expressed in terms of S_P as

$$S_i = \left(\frac{qv}{L}\right)^2 S_P \tag{5.5}$$

In the absence of an applied field, the diffusion length, L_D, is the distance a free carrier diffuses before recombining into quantum well ground states. Therefore, the current noise in the diffusion dominant regime can be expressed as

$$S_i = 4q^2\overline{G}\left(\frac{\tau_0 v}{L}\right)^2 = 4q^2\overline{G}\left(\frac{L_D}{L}\right)^2 \tag{5.6}$$

When a sufficiently large electric field is applied, the transport mechanism becomes drift dominated and Eq. (5.6) is no longer valid. By using Eq. (5.2), Eq. (5.4), and Eq. (5.5), the current noise spectral density can then be expressed as

$$S_i = \frac{4q^2}{\overline{G}}\frac{P_0^2}{(\frac{L}{v})^2} = \frac{4I_d^2}{\overline{G}} \tag{5.7}$$

As a result, the current noise in the drift dominant regime is proportional to the dark current squared and inverse proportional to the total hole generation rate.

5.5.2 Hole generation rate

Considering quantum well ground states as the trap states for the holes in the valence band extended states, the generation rate density, $\overline{g}$, can be expressed as

$$\overline{g} = N_a v_{th} \sigma_p N_v e^{(-\frac{E_0 - E_v}{kT})} \tag{5.8}$$

where N_a is the doping density in the quantum well, nearly equal to the trapped hole concentration, v_{th} is the hole thermal velocity, σ_p is the cross-sectional area for hole trapping into the quantum well ground states, and N_v is the effective density of states of the valence band. E_v and E_0 are the valence band extended state energy and quantum well ground state energy, respectively. For a p-type QWIP with doped quantum wells and undoped barriers, the total hole generation rate can be expressed in terms of generation rate density as $\overline{G} = NAL_w\overline{g}$, where L_w is the width of a quantum well.

In equilibrium, the energy barrier seen by the holes in the quantum well ground states is $E_b = E_0 - E_v$. With an electric field present in the well, the energy band diagram will be tilted and the effective energy barrier on the cathode side of the quantum well will be reduced by approximately $\Delta E_{\mathcal{E}} = q\mathcal{E}L_w$, where $\mathcal{E}$ is the electric field in the well. This barrier lowering effect due to the electric field will cause an increasing in the hole generation rate when a bias voltage is applied to the device.

In addition, the image-force-induced barrier lowering should be taken into account because of the highly doped state of the quantum wells. When a hole is in the barrier region at a distance x from the quantum well/barrier interface, the image force is given by Schottky[34] as

$$F = \frac{-q^2}{4\pi(2x)^2\epsilon_0\epsilon_r} = \frac{-q^2}{16\pi\epsilon_0\epsilon_r x^2} \tag{5.9}$$

where q is the hole charge, ϵ_0 is the permittivity in vacuum, and ϵ_r is the dielectric constant of the barrier. When the external field $\mathcal{E}$ is applied, the total potential energy PE as a function of distance [with $PE(x \to \infty)|_{\mathcal{E}=0} = 0$] is

$$PE(x) = \frac{q^2}{16\pi\epsilon_0\epsilon_r x} + q\mathcal{E} \cdot x \tag{5.10}$$

The Schottky barrier lowering $q\Delta\phi$ is given by the condition $\frac{d[PE(x)]}{dx} = 0$, resulting in

$$q\Delta\phi = q\sqrt{\frac{q\mathcal{E}}{4\pi\epsilon_0\epsilon_r}} \tag{5.11}$$

To have a significant Schottky effect, holes inside the quantum well must be able to form a charge plane (image plane) during the hole escape process[23]. Therefore, the dielectric relaxation time, τ_{rel}, in the Fermi sea must be much smaller than the hole escape time, τ_{esc}, i.e.,

$$\tau_{esc} \gg \tau_{rel} = \epsilon_0\epsilon_r\rho = \frac{\epsilon_0\epsilon_r}{q\mu p} \tag{5.12}$$

where ρ is the resistivity and μ is the hole mobility.

For our p-type QWIP with a quantum well doping concentration of $2 \times 10^{18} cm^{-3}$, the dielectric relaxation time for a heavy hole is approximately $7 \times 10^{-15} sec$ by assuming bulk GaAs heavy hole parameter values. On the other hand, the escape time can be estimated from the time it takes an hole to pass through a single barrier region.

$$\tau_{esc} \approx \frac{L_b}{\overline{v}} \tag{5.13}$$

where $\overline{v} = \sqrt{\frac{3kT}{m}}$ is the average hole velocity. With a 500 Å barrier width, the escape time is approximately $6 \times 10^{-13} sec$ at 80K and $5 \times 10^{-13} sec$ at 130K by assuming, again, bulk GaAs parameter values. This first order calculation shows that τ_{rel} is significantly smaller than τ_{esc} indicating that indeed the Schottky effect needs to be accounted for.

The total energy barrier lowering ΔE, including both the electric field effect and the Schottky image effect, becomes

$$\Delta E = q\Delta\phi + q\mathcal{E}L_w \quad (5.14)$$

The total hole generation rate is then

$$\overline{G} = NAL_w\overline{g} = NAL_wN_av_{th}\sigma_pN_ve^{(-\frac{E_b-\Delta E}{kT})} = NAL_wCe^{(-\frac{E_b-\Delta E}{kT})} \quad (5.15)$$

In the following we will neglect a possible weak temperature or field dependence of the parameter C.

5.6 Device Parameter Extraction

5.6.1 Comparison between current noise and experimental data

The expression for the noise current plateau values in the drift dominant regime can be written, using Eq. (5.15), as

$$S_i = \frac{4I_d^2}{NAL_wCe^{(-\frac{E_b-\Delta E}{kT})}} \quad (5.16)$$

Assuming a position independent electric field, the hole generation rate constant, C, was found by fitting Eq. (5.16) to the measured noise data in the drift dominant regime resulting in $C = 9.4 \times 10^{30}cm^{-3}s^{-1}$. Fig. 5.9 shows the measured noise plateau values versus applied reverse bias voltage for different temperatures and the results of our fit(solid lines). Note that Eq. (5.16) explains the magnitude of the noise and its current dependency very well for all temperatures considered.

Once the generation rate constant has been determined, the noise current spectral density in the diffusion dominant regime, written as

$$S_i = 4q^2NAL_wCe^{(-\frac{E_b-\Delta E}{kT})}\left(\frac{L_D}{L}\right)^2 \quad (5.17)$$

can be used to determine L_D by fitting Eq. (5.17) to the measured noise data in this regime. The low field diffusion length, L_D, was found to be 450 Å. With this value

for L_D, the current noise spectral densities in the diffusion dominant regime were calculated and plotted in Fig. 5.9, using the dashed lines, for different temperatures showing that there is a good agreement between theory and experiment in terms of noise magnitude and its current dependence for all temperatures considered.

5.6.2 Capture cross-section for hole trapping in the quantum well ground states

From the drift dominant current noise component we found:

$$C = N_a N_v v_{th} \sigma_p = 9.4 \times 10^{30} \qquad cm^{-3} s^{-1}$$

To explain this value of C and derive a value of σ_p within the context of the hole transport mechanism and the quantum well characteristics we propose the following model.

The thermally generated heavy holes will move via drift or diffusion in the barrier region to a neighboring quantum well. These quantum wells are doped with Beryllium acceptors to a concentration of $2 \times 10^{18} cm^{-3}$, which results in an inter acceptor spacing of about 100 Å. Since the well width L_w is only 48 Å, these acceptors basically form a monolayer thin plane of nearly neutral charge centers. The holes approaching this monolayer with a thermal velocity determined by barrier parameters will interact with these Be-centers triggering a recombination process which results in the holes reaching the HH1 bound states. Assuming ineffective screening of the Be nuclei due to the two dimensionality of the surrounding electron gas, we approximate the Be perturbation potential by[49] $\frac{Zq}{4\pi\epsilon_0\epsilon_r r}$ where Z is the atomic number of Be, equal to 4. The holes impinging on the Be-centers gain kinetic energy by crossing the barrier/well interface. Hence to determine the effective scattering cross section, σ_p, of the Be-centers embedded in the quantum wells we equate

$$\frac{Zq^2}{4\pi\epsilon_0\epsilon_r r} = E_b + E_{th} \tag{5.18}$$

from which $\sigma_p = \pi r^2$ can be calculated. $E_{th} = kT$ is the thermal energy of the holes in

the barrier region. This equation reflects that holes with energy less than the total energy, stated in the right hand side of Eq. (5.18), are subject to scattering, triggering a recombination process whereas holes with energies higher than the energy stated do not sense the perturbation potential and continue their path unperturbed.

Selecting a temperature near the middle of our temperature range, we calculate, at T=100K, that $\sigma_p(100K) = 1.9 \times 10^{-13} cm^2$. The measured value for σ_p follows from $C = N_a N_v v_{th} \sigma_p = 9.4 \times 10^{30} cm^{-3} s^{-1}$. Using $N_a = 2 \times 10^{18} cm^{-3}$ and bulk GaAs values for N_v and v_{th}, we find at 100K

$$\sigma_{p_{exp}} = 2.6 \times 10^{-13} cm^2$$

which is in good agreement with the predictions of the model outlined above.

5.7 Conclusion

The dark current noise measurements show that the noise of the p-type QWIP under study can be attributed to number fluctuation noise associated with the generation and recombination of holes from and to the quantum well ground states and the valence band extended states. At low bias voltage, the number fluctuation noise translates into current fluctuation noise via the diffusion mechanism. When the applied bias increases, charge transport becomes drift dominant and the number fluctuation noise couples to current noise via the hole drift mechanism resulting in a strong current dependence.

In addition, we found that the stress in the device does not generate a significant amount of excess noise. Inspection of the measured spectra indicates that the excess corner frequency lies below 100 Hz for the QWIP under study. Using the model presented in this chapter, the low field diffusion length was extracted to be 450 Å which indicates that holes thermally generated in a quantum well travel, on average, one period before they trap into nearest neighbor quantum wells. This trapping

process is triggered by hole scattering with Be acceptor centers of which the scattering cross-section was measured to be $\sigma_p = 2.6 \times 10^{-13} cm^2$.
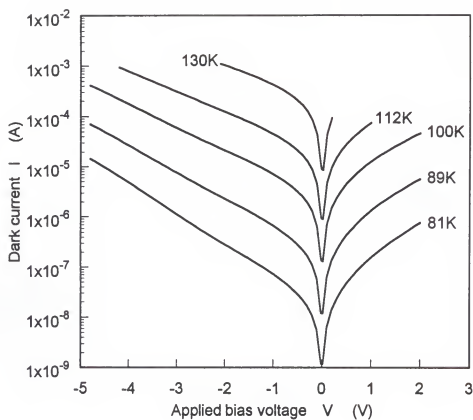
Figure 5.1 Dark current versus applied bias voltage for different temperatures.
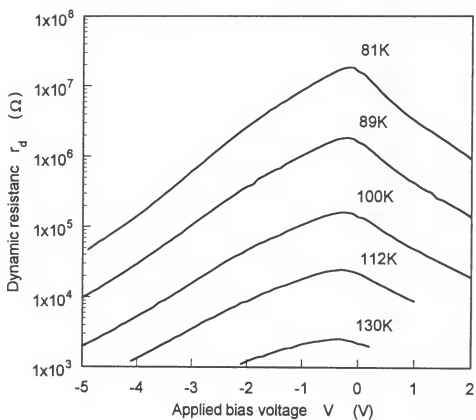
Figure 5.2 Dynamic resistance versus applied bias voltage for different temperatures.
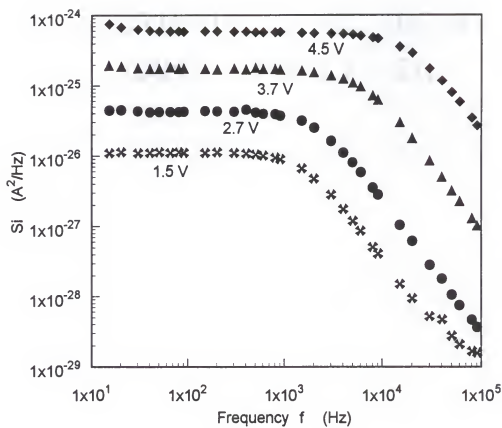
Figure 5.3 Current noise spectral density versus frequency at 81K.
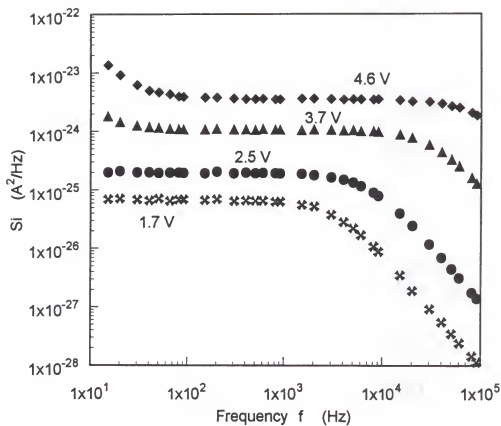
Figure 5.4 Current noise spectral density versus frequency at 89K.
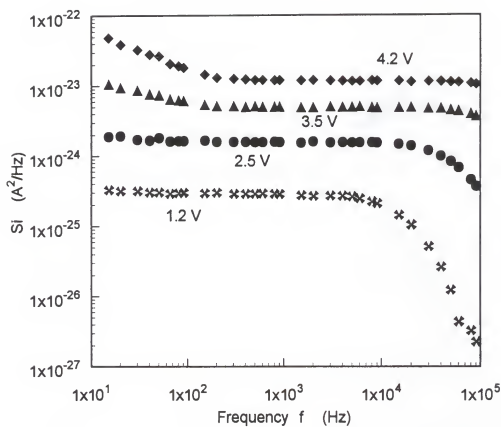
Figure 5.5 Current noise spectral density versus frequency at 100K.
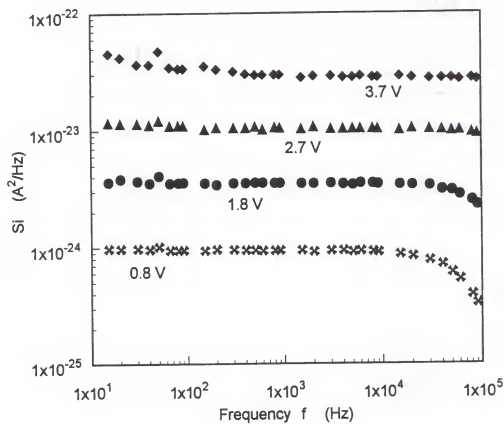
Figure 5.6 Current noise spectral density versus frequency at 112K.
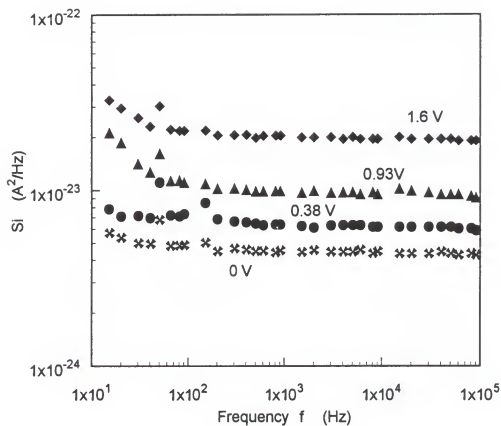
Figure 5.7 Current noise spectral density versus frequency at 130K.
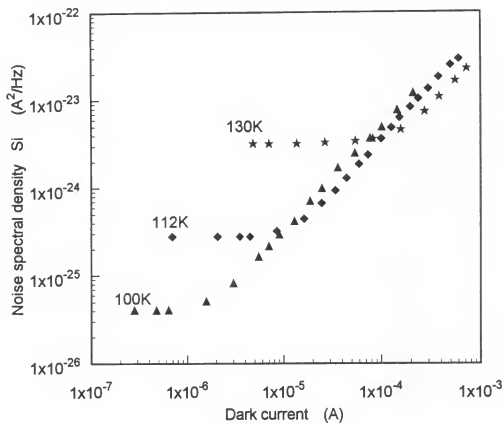
Figure 5.8 Current noise spectral density versus dark current for different temperatures.
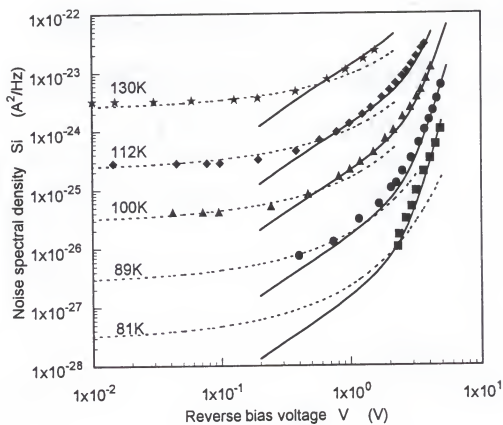
Figure 5.9 Experimental and theoretical current noise spectral density versus bias voltage for different temperatures.

CHAPTER 6
QWIP DESIGN CRITERIA

6.1 Introduction

To evaluate the performance of a QWIP, the specific detectivity (D^*) is the most often used figure of merit. In a QWIP design, D^* maximization is an important issue to ensure a good performance. Some articles focus on increasing the responsivity by increasing the quantum efficiency[51] while others discuss reducing the current noise by reducing the dark current[16]. However, most of the study address aspects of novel QWIP structures. There is no systematic study on the dependence of the design parameters as they apply to a more or less standard QWIP.

The purpose of this chapter is to find the effects on D^* caused by a change in design parameters. Therefore, a simplified D^* expression will be derived. In this model the following three parameters are the adjustable design parameters which effect the value of the detectivity; number of quantum wells, doping concentration of the quantum wells, and the effective mass of the mobile carrier.

Using the measured QWIP data, the dependency of D^* on these three design parameters was obtained. Subsequently, D^* values were calculated and plotted as a function of these design parameters revealing that a maximum in D^* can be achieved.

6.2 Specific Detectivity of QWIPs

6.2.1 Definition of the specific detectivity D^*

Let us assume that the QWIP acts as an ideal photodetector. If IR radiation with a constant power $\overline{P}$ is incident upon a QWIP, the photocurrent generated by this incoming photon stream is

$$I_p = q\eta \frac{\overline{P}}{\hbar\omega} g_{op} \tag{6.1}$$

where q is the charge of the mobile carrier, ω is the radian frequency of the incident photon, η is the quantum efficiency, and g_{op} is the photocurrent gain of the QWIP[53]. The current responsivity is defined as the ratio of the photocurrent over the power of the incident photon flux. In the actual measurement, the incident photon flux is usually chopped resulting in a current responsivity dependent on photon radian frequency, ω, as well as on chopping frequency f.

$$R(\omega, f) = \frac{I_p}{\overline{P}} = \frac{q\eta g_{op}}{\hbar\omega} \tag{6.2}$$

In order to calculate D^*, the noise equivalent power (P_{eq}) needs to be calculated first. By definition, P_{eq} is the input optical power for which the signal-to-noise ratio equals one. Using Eq. (6.2), the noise equivalent power is

$$P_{eq}(\omega, f, \Delta f, A) = \frac{\sqrt{S_i(f)\Delta f}}{R(\omega, f)} = \frac{\hbar\omega\sqrt{S_i(f)\Delta f}}{q\eta g_{op}} \tag{6.3}$$

where, $S_i(f)$ is the total current noise spectral density of the QWIP and A is the device area.

Since the specific detectivity is the inverse of the noise equivalent power when $\Delta f = 1$ Hz and $A = 1$ cm^2, we have

$$D^*(\omega, f) = \frac{1}{\frac{P_{eq}(\omega, f, \Delta f, A)}{\sqrt{A\Delta f}}} = \frac{q\eta g_{op}\sqrt{A}}{\hbar\omega\sqrt{S_i(f)}} \tag{6.4}$$

6.2.2 Current gain and current noise spectral density

The noise components contributing to the overall output current noise of a QWIP can be classified into three categories: The current noise, denoted as $S_i^{(b)}$, is produced by the blackbody background photon field. The noise, $S_i^{(op)}$, stemming from incident radiation is called photoinduced signal noise. The third noise component is independent of the photon field and is called spontaneous device noise $S_i^{(sp)}$. The total QWIP noise, measured at the device terminals, is equal to the superposition of these three noise sources.

For most of the QWIPs, the current gain is much less than one and they are operated in the non-BLIP regime resulting in $S_i^{(op)}$ and $S_i^{(b)}$ much less than $S_i^{(sp)}$. The overall current noise, S_i, then can be approximated by the device noise $S_i^{(sp)}$. Using the noise model presented in chapter 5, the expression for the noise current plateau values in the drift dominant regime is

$$S_i = \frac{4I_d^2}{NAL_w\overline{g}} \tag{6.5}$$

where I_d is the dark current, N is the number of quantum wells, L_w is the width of the quantum well, and $\overline{g}$ is the thermal carrier generation rate density. Since the noise gain is identical to photocurrent gain in this regime of operation, g_{op} can be calculated as

$$g_{op} = \frac{S_i}{4qI_d} = \frac{I_d}{qNAL_w\overline{g}} \tag{6.6}$$

To calculate the effective absorption length for incident light, we need to consider the following QWIP features: Due to the structure of QWIP, only the quantum wells absorb incident radiation. In addition, multiple reflection at the interface of semiconductor and air leads to a number of passes, m, of the incident photon through the QWIP. The total distance for absorption becomes mNL_w. If the absorption

coefficient for a QWIP quantum well is α, the quantum efficiency can be expressed as

$$\eta = 1 - e^{-mNL_w\alpha} \tag{6.7}$$

As a result, D^* from Eq. (6.4) can be expressed as

$$D^* = \frac{1 - e^{-mNL_w\alpha}}{2\hbar\omega\sqrt{NL_w\bar{g}}} \tag{6.8}$$

6.3 Absorption Coefficient

To calculate the absorption coefficient α, knowledge about the wavefunction of a carrier in the quantum wells is required. Since the purpose of this chapter is to find the parameters to maximize the specific detectivity, a simplified model for absorption is presented in this section. Using this model, the dependency of the absorption coefficient on the design parameters is determined.

6.3.1 General expression for the photon induced transition probability

The Hamiltonian for the interaction between the incident radiation and the carrier can be written as[54]

$$H_{ex} = q\mathbf{A}\,\overset{\leftrightarrow}{W}\,\mathbf{P} \tag{6.9}$$

where, q is the charge of the carrier, $\mathbf{A} = \mathbf{A}_0 e^{i\omega t}$ is the vector potential of the incident light, $\mathbf{P}$ is the momentum operator, $\overset{\leftrightarrow}{W}$ is the 3x3 inverse effective mass tensor taking into account the anisotropic nature of the band structure. Without illumination, the wavefunction of a carrier at the energy state E_n is Ψ_n. Once the system is perturbed by incident radiation, the transition probability of a carrier between the ground state, E_0, and the mth excited state, E_m, using first-order perturbation theory, is given by

$$|a_m|^2 = \frac{|H_m|^2}{\hbar^2(\Omega_m^2 + 1/4\tau^2)} \tag{6.10}$$

where $H_m = <\Psi_m|H_{ex}|\Psi_0>$, $\hbar\Omega_m = E_m - E_0 - \hbar\omega$, and τ is the lifetime of the carrier in the mth excited state.

If we define the growth direction of the sample as z axis and the plane perpendicular to this direction as the xy plane, the wavefunction of the mth excited state is

$$\Psi_m(\mathbf{k}) = \phi_m(z)u(\mathbf{r})e^{i\mathbf{k}\cdot\rho} \tag{6.11}$$

where $u(\mathbf{r})$ is the Bloch function, and $\mathbf{k} = (k_x, k_y)$ and ρ are the wave vector and coordinate in the xy plane, respectively. $\phi_m(z)$ is the envelope function and satisfies the following condition:

$$\left[\frac{-W_{zz}\hbar^2}{2}\frac{\partial^2}{\partial z^2} + V(z)\right]\phi_m(z) = E_m\phi_m(z) \tag{6.12}$$

where $V(z)$ is the potential energy. In a QWIP, the intersubband transition occurs only when the momentum is conserved in the xy plane. For the transition between the ground state and the mth excited state, the perturbation H_m is

$$H_m = <\Psi_m(\mathbf{k})|q\mathbf{A}\overleftrightarrow{W}\mathbf{P}|\Psi_0(\mathbf{k})> = q\sum_{i=x,y,z}A_iW_{iz}<\phi_m|P_z|\phi_0> \tag{6.13}$$

The average transition probability per unit time can be expressed as a function of H_m,

$$g_m(\mathbf{k}) = \frac{|a_m|}{\tau} = \frac{|H_m|^2}{\hbar^2(\Omega_m^2 + 1/4\pi^2)\tau} \tag{6.14}$$

Let us assume that the energy band in the xy plane can be approximated as parabolic resulting in $E_m(\mathbf{k}) - E_0(\mathbf{k}) = E_m - E_0$. In addition, since the Fermi energy E_f is far below the first excited state E_1 we have $f[E_m(\mathbf{k})] \approx 0$ and the density of states in the k-plane including the spin degeneracy is $2/(2\pi)^2$ per unit area. The probability of a carrier scattered away from the ground state into the mth excited state becomes[55]

$$g_m = \int_{\mathbf{k}} \frac{2d\mathbf{k}}{(2\pi)^2}f[E_0(\mathbf{k})]g_m(\mathbf{k}) \tag{6.15}$$

where $f[(E_0(\mathbf{k})]$ is the Fermi distribution function. If we introduce a two dimensional density of states $N_0[E(\mathbf{k})]$, the integration can be carried out over the energy space,

$$g_m = \int_{E_0}^{\infty} dE(\mathbf{k}) N_0[E(\mathbf{k})] g_m(\mathbf{k})$$

$$= \frac{q^2 N_s}{[(E_m - E_0 - \hbar\omega)^2 + \hbar^2/4\tau^2]\tau} \left| \sum_i A_i W_{iz} < \phi_m |P_z| \phi_0 > \right|^2 \quad (6.16)$$

where $N_s = \int_{E_0}^{\infty} dE(\mathbf{k}) N_0[E(\mathbf{k})] f[E_0(\mathbf{k})]$ is the sheet density of the carriers in the quantum well.

6.3.2 A simplified model for the absorption coefficient

Due to the structure of the QWIP, i.e. doped quantum wells and undoped barriers, only quantum wells absorb the incident radiation. By definition, the absorption coefficient is the energy absorbed per unit time in a unit volume divided by the energy flux. Therefore, the absorption coefficient of a QWIP is[55]

$$\alpha(\omega) = \frac{\hbar\omega g_m}{p L_w} \quad (6.17)$$

where, $p = c\epsilon_s A^2 \omega^2/2$ is the average energy flux of the radiation, ϵ_s is the permittivity of the quantum well, and c the velocity of the light in free space.

Consider a simplified case in which the energy barriers of the quantum wells are infinite and the $\overleftrightarrow{W}$ tensor has no off-diagonal elements. The perturbation for a transition from ground state to the first excited state is[56]

$$H_1 = q \sum_{i=x,y,z} A_i W_{iz} < \phi_1 |Pz| \phi_0 >= q \frac{A}{m^*} \frac{8\hbar}{3 L_w} \quad (6.18)$$

where $W_{zz} = 1/m^*$ and $A = A_z$. The absorption coefficient $\alpha|_{\hbar\omega=(E_1-E_0)}$ becomes

$$\alpha = \frac{512 \hbar q^2 N_s \tau}{9 c \epsilon_s \omega L_w^3 m^{*2}} \quad (6.19)$$

If the energy, E, of a carrier is $\frac{\hbar^2 k^2}{2m^*}$, the lifetime, τ, can be estimated from the uncertainty principle, $\Delta E \cdot \tau \geq \hbar/2$. Therefore,

$$\tau \geq \frac{\hbar}{2\Delta E} = \frac{m^*}{2\hbar k \Delta k} \quad (6.20)$$

The uncertainty principle in the momentum space states that $\Delta x \cdot \Delta k \geq 1/2$. Since the carrier is confined in the quantum well resulting in $\Delta x = L_w$, the uncertainty Δk is $\frac{1}{2L_w}$. Using Eq. (6.20), the lifetime can be approximated as

$$\tau \approx \sqrt{\frac{m^*}{2\hbar\omega}} L_w \tag{6.21}$$

Assuming carriers in a QWIP are fully ionized and occupy the quantum well ground state, the sheet density is approximately equal to $N_d L_w$, where N_d is the doping concentration of the wells. The absorption coefficient becomes

$$\alpha = \frac{256\sqrt{2\hbar}q^2 N_d}{9c\epsilon_s L_w (\omega m^*)^{3/2}} \tag{6.22}$$

From the above simplified absorption coefficient, D^* can be written as a function of N, N_d, and m^*.

$$D^* = \frac{1 - e^{-mNL_w \frac{256\sqrt{2\hbar}q^2 N_d}{9c\epsilon_s L_w (\omega m^*)^{3/2}}}}{2\hbar\omega\sqrt{NL_w \overline{g}}} \tag{6.23}$$

6.4   Detectivity Maximization

Based on the D^* expression in the previous section, three parameters, namely the number of quantum wells (N), doping concentration (N_d), and the effective mass (m^*), can be independently adjusted for optimal QWIP design. In this section, a p-type strained layer QWIP is examined to investigate the results of parameter variation. Table 6.1 lists the actual device parameters of this QWIP, where ϵ_r is the dielectric constant.

Since this QWIP has no antireflection (AR) coating on the surface of the QWIP, the power transmission from air into the device is about 70%. Once the transmitted light passes through the QWIP, upon the reflection at the top semiconductor/gold contact interface, over 90% of the internal power will be reflected back into the QWIP. When this reflected light passes through the QWIP and reaches the semiconductor/air interface, only 30% of the internal power will be reflected again back into the

QWIP. After three internal reflections at the semiconductor/gold contact interface and two internal reflections at the semiconductor/air interface (m=6), the power of the reflected radiation will drop below 4.5% of the initial incident power. Using the parameters in Table 6.1, the absorption coefficient calculated from Eq. (6.22) is 1500 cm^{-1}. In a QWIP, the excited state is delocalized so that the photocarriers are more mobile than in the ideal quantum well system resulting in a longer carrier lifetime. Therefore, the absorption coefficient of a QWIP is smaller than the estimated value from Eq. (6.22). In this section, three arbitrary α values, 500, 1000, and 1500 cm^{-1} are selected for the calculation to cover the most practical ranges of the absorption coefficient of QWIPs.

6.4.1 Dependency on the number of quantum wells

Using Eq. (6.8) and the parameters listed in Table 6.1, D^* versus N is plotted in Fig. 6.1 for three α values. The D^* value increases an order of magnitude when the number of quantum wells increases from 1 to 50. Once N is larger than 50, the increase of D^* slows down. For example, D^* value increases only 50% from $N = 50$ to $N = 200$ for $\alpha = 1000$ cm^{-1}. In practice, for a QWIP without AR coating treatment on the device surface, it is not worth to increase the number of quantum wells beyond $N = 50$.

6.4.2 Dependency on the doping concentration

From chapter 5, the carrier generation rate is a function of doping concentration,

$$\overline{g} = N_d v_{th} \sigma N_c e^{-E_b/kT} = C_1 N_d \tag{6.24}$$

If the absorption coefficient in Eq. (6.22) can be expressed as $\alpha = C_2 N_d$, D^* in Eq. (6.23) can be written as

$$D^* = \frac{1}{2\hbar\omega\sqrt{NL_w}} \frac{1 - e^{-mNL_w C_2 N_d}}{\sqrt{C_1 N_d}} \tag{6.25}$$

C_1 is calculated to be 500 s^{-1} at 100K based on the parameters listed in Table. 6.1. Figure 6.2 shows D^* versus doping concentration for three different α values and the corresponding C_2 values are 2.5×10^{-16}, 5.0×10^{-16}, and 7.5×10^{-16} cm^2, respectively. According to Fig. 6.2, the specific detectivity increases when the doping concentration increases until D^* reaches a maximum. The maximum in D^* occurs around $N_d = 3 \times 10^{19} cm^{-3}$. For a smaller absorption coefficient a higher doping concentration is required to maximize the detectivity.

6.4.3 Dependency on the effective mass

The effective mass m^* of the quantum well depends on the composition of the ternary materials used in the QWIP quantum well formation. The energy state in a quantum well with infinite energy barrier is $E_n = \frac{\pi^2 \hbar^2}{2 L_w^2 m^*}(n+1)^2$. For the transition from ground state, E_0, to the first excited state, E_1, the photon energy for maximum absorption is

$$\hbar\omega = E_1 - E_0 = \frac{3\pi^3 \hbar^2}{2 L_w^2 m^*} \tag{6.26}$$

resulting in

$$L_w = \pi \sqrt{\frac{3\hbar}{2\omega}} \frac{1}{\sqrt{m^*}} = C_3 m^{*-1/2} \tag{6.27}$$

If we assume that the dielectric constant of the quantum well is nearly constant for most of the QWIPs, the absorption coefficient can be expressed as a function of effective mass,

$$\alpha = \frac{512 q^2 N_d}{9\sqrt{3} \pi c \epsilon_s \omega m^*} = C_4 m^{*-1} \tag{6.28}$$

If we approximate $v_{th} = \sqrt{3kT/m^*}$ and $N_c = 2(2\pi m^* kT/h^2)^{3/2}$, the coefficient of the thermal carrier generation rate density in terms of the effective mass is

$$\overline{g} = 2 N_d \sqrt{\frac{3kT}{m^*}} \sigma \left(\frac{2\pi m^* kT}{h^2} \right)^{3/2} e^{\frac{-E_b}{kT}} = C_5 m^* \tag{6.29}$$

As a result, D^* in Eq. (6.23) can be written as

$$D^* = \frac{1 - e^{-mNC_3 C_4 m^{*-3/2}}}{2\hbar\omega \sqrt{NC_3 C_5} m^{*1/4}} \tag{6.30}$$

For this p-type QWIP at 100K, C_3 equals 1.0×10^{-21} cm $\sqrt{g}$ and C_5 equals 2.2×10^{48} $cm^{-3}s^{-1}g^{-1}$. The C_4 values for three different absorption coefficients are 2.25×10^{-31}, 4.50×10^{-31}, and 6.75×10^{-31} $cm^{-1}g^{-1}$, respectively. Fig. 6.3 shows the plot of D^* versus m^*. The upper limited of the m^* value is set by the heavy hole mass of GaAs and the lower one by InAs. Obviously, smaller effective mass values result in a larger D^*.

6.5   Design Criteria

From the previous analysis of the spectral specific detectivity, the following criteria can be derived and used as a guideline for a QWIP designer:

- For QWIPs with no surface treatment, the best choice for the quantum well number ranges from 20 to 50 depending on the value of the absorption coefficient. The larger the absorption coefficient, the smaller the N value requires to give a relative large D^*.

- The doping concentration of the quantum wells needs to be chosen around 3×10^{19} to 1×10^{20} cm^{-3} to obtain a maximum in D^*. Figure 6.2 shows that a smaller absorption coefficient value in a QWIP requires a higher doping concentration to reach the maximum D^*. For the n-type QWIPs, due to the limitation of MBE technology, the doping concentration can not increase up to $10^{20}cm^{-3}$. In that case, N_d needs to be chosen as high as possible.

- The effective mass in the quantum wells is determined by the materials used in the QWIP quantum well formation. Obviously, a smaller effective mass gives a better specific detectivity. In general, the heavy hole mass in InAs is about $0.35m_0$ and the heavy hole mass in GaAs or AlAs is about $0.5m_0$. From our analysis, an increase in the Indium percentage in the InGaAs ternary will lower the effective mass and results in a better detectivity. The situation is similar

for n-type QWIPs because the effective mass in InAs is also the smallest among the materials available.

Table 6.1: Parameters of the p-type strained layer QWIP.

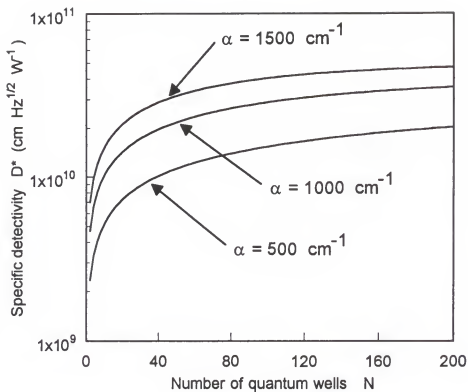| T (K)	$\hbar\omega$ (eV)	N	N_d (cm^{-3})	L_w (Å)	m^* (m_0)	g ($cm^{-3}s^{-1}$)	ϵ_r
100	0.124	20	2×10^{18}	48	0.5	10^{21}	13.2

Figure 6.1 Specific detectivity (D*) vs. number of quantum well (N) for three different values of absorption coefficient(α).
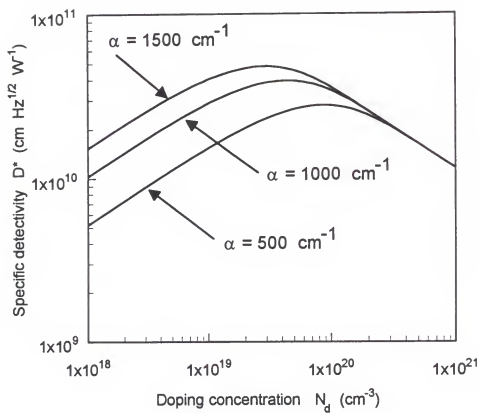
Figure 6.2 Specific detectivity (D*) vs. quantum well doping concentration (N_d)
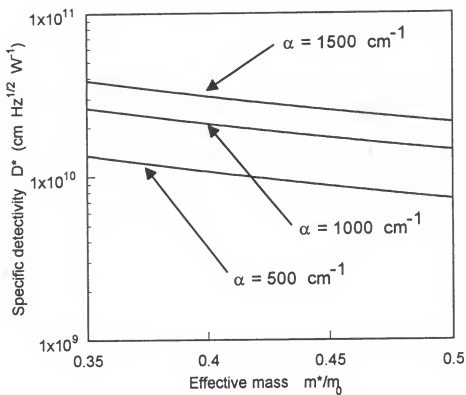for three different values of absorption coefficient (α).

Figure 6.3 Specific detectivity (D*) vs. quantum well effective mass (m*) for three different values of absorption coefficient (α).

CHAPTER 7
CONCLUSIONS AND RECOMMENDATIONS

7.1 <u>Conclusions</u>

In this dissertation, studies of both the QWIP's dark current and noise characteristics have been carried out. Several conclusions can be drawn from our results.

- The current-voltage characteristic of a BTM QWIP can be modelled using a modified thermionic emission theory coupled with an image lowering effect. Good agreements between the modelled and measured dark current indicate that the charge transport process is emission limited. Our dark current studies clarify the vague understanding of the QWIP's transport mechanism.

- Dark current noise measurements between 10^1 and 10^5 Hz were carried out for different types of III-V QWIPs at different temperatures. The noise level is independent of frequency at low and medium applied bias voltages which are used in the operation of the QWIPs. When the bias voltage increases to causing a significant amount of current to flow through the device, 1/f-like noise becomes large and starts to dominate the spectra. In general, an IR detector should operate at a bias voltage and electrical frequency where 1/f-like noise is absent to ensure good noise performance. Our noise measurements provide these voltage and frequency ranges for operation.

- The measured spectra indicate that stress in the QWIPs we measured does not generate a significant amount of excess noise. Even the strain introduced in the

p-type QWIP on purpose to enhance normal incident IR radiation absorption does not degrade its noise performance. As a matter of fact, good interface quality can be achieved even with such an intended strain in the p-type QWIPs.

- The noise plateau levels are attributed to number fluctuation noise associated with the generation and recombination of carriers from and to the quantum well ground states and the extended continuous states. In equilibrium, the current noise spectral density of the g-r noise conforms to the well-known Nyquist expression.

- At low bias voltage the number fluctuation noise translates into current fluctuation noise via the diffusion mechanism. When the applied bias increases, charge transport becomes drift dominant and the number fluctuation noise couples to current noise via the drift mechanism resulting in a strong current dependence of the current noise plateau level.

- A noise model based on priori known quantities was developed to predict the current noise levels in both diffusion and drift limited regimes. Based upon this model, the low field carrier diffusion length and the capture cross section for carrier trapping in the quantum wells could be extracted from the noise data.

- The trapping process of carriers travelling through the quantum well regions is triggered by carriers scattering with the donor or acceptor centers. Carriers with an energy lower than the donor or acceptor perturbation potential energy are subject to scattering which triggers a recombination process whereas carriers with higher energies do not sense the perturbation potential and continue their path unperturbed.

- Under low applied bias voltage, carriers are thermally generated from the quantum well ground states and then travel, on the average, one or two periods before they trap into the neighboring quantum wells. In general, the carrier

lifetime in the quantum well bound states is much larger than the intra-well carrier scattering time allowing the carriers to fully thermalize in the quantum wells. The thermalization process decouples the statistical fluctuations in carrier transport through a barrier region from one section to the next. Therefore, a QWIP can be considered as M statistically independent sections in series, where M is equal to the ratio of active device length over the extended state carrier trajectory.

- Maximum detectivity can be achieved by properly adjusting the design parameters such as doping concentration and number of the quantum wells. In order to have a large detectivity, materials with a small effective mass are recommended for forming the quantum wells.

7.2 Suggestions for Further Research

Extensions of this research are proposed as follows:

1. The carriers inside the quantum wells are generated by either thermal or photo excitation processes. Once the carriers are generated, they experience the same transport mechanism, independent of their excitation source. In equilibrium, a generated carrier has equal probability for transferring to the next quantum well on the anode or cathode side resulting in a zero mean current in the external circuit. Therefore, at zero bias the optical gain is zero while the noise gain which is an a.c. quantity is not. At larger bias voltage, all the generated carriers move in one direction, the noise gain and optical gain becomes identical. Further study should focus on finding the noise gain interpretation under equilibrium and low bias voltage condition.

2. Infrared imaging is the main purpose for fabricating and studying QWIPs. Many researchers have focused on design and fabrication of Infrared Focal Plane

Array (FPA) systems[57]–[59]. In this dissertation, our studies mainly addressed on the single device level. The next step of study should focus on the system level of FPA using QWIPs as the detecting elements and emphasize on such issues as noise equivalent temperature difference (NETD), detectivity uniformity, and FPA system design.

REFERENCES

[1] W. Herschel, Phil. Trans. R. Soc. **90**, 284, 477 (1800).

[2] L. C. West and S. J. Eglash, Appl. Phys. Lett. **46**, 1156 (1985).

[3] Larry S. Yu, Sheng S. Li, and Pin Ho, Appl. Phys. Lett. **59**, 2712 (1991).

[4] Larry S. Yu, Y. H. Wang, Sheng S. Li, and Pin Ho, Appl. Phys. Lett. **60**, 992 (1992).

[5] Larry S. Yu, Sheng S. Li, Y. H. Wang, and Y. C. Kao, J. Appl. Phys. **72**, 2105 (1992).

[6] Y. H. Wang, Sheng S. Li, and Pin Ho, Appl. Phys, Lett. **62**, 621 (1993)

[7] B. F. Levine, C. G. Bethea, G. Hasnain, V. O. Shen, E. Pelvé, R. R. Abbott, and S. J. Hsieh, Appl. Phys. Lett. **56**, 851 (1990).

[8] A. Zussman, B. F. Levine, J. M. Kuo, and J. deJong, J. Appl. Phys. **70**, 5101 (1991).

[9] B. F. Levine, A. Zussman, S. D. Gunapala, M. T. Asom, J. M. Kuo, and W. S. Hobson, J. Appl. Phys. **72**, 4429 (1992).

[10] K. K. Choi, L. Fotiadis, M. Taysing-Lara, W. Chang, and G. J. Iafrate, Appl. Phys. Lett. **60**, 592 (1992).

[11] J. Y. Andersson, L. Lundqvist, and Z. F. Paska, Appl. Phys. Lett. **58**, 2264 (1991).

[12] A. Köck, E. Gornik, G. Abstreiter, G. Böhm, M. Walther, and G. Weimann, Appl. Phys. Lett. **60**, 2011 (1992).

[13] L. J. Kozlowski, G. M. Williams, G. J. Sullivan, C. W. Farley, R. J. Anderson, J. Chen, D. T. Cheung, W. E. Tennant, and K. E. Dewames, IEEE Trans. Electron Devices **38**, 1124 (1991).

[14] L. Esaki and R. Tsu, IBM J. Res. Dev. **14**, 61 (1970).

[15] L. Esaki and L. L. Chang, Phys. Rev. Lett. **33**, 495 (1974).

[16] K. K. Choi, L. Fotiadis, M. Taysing-Lara, and W. Chang, Appl. Phys. Lett. **59** 3303 (1991).

[17] D. Teng, C. Lee, and L. F. Eastman, J. Appl. Phys. **72**, 1539 (1992).

[18] Y. H. Wang, Sheng S. Li, and J. Chu, Appl. Phys. Lett. **64**, 727 (1994).

[19] Y. H. Wang, J. Chu, and Sheng S. Li, J. Appl. Phys. **76**, 6009 (1994).

[20] L. Dapkus, V. Jasutis, S. Kačiulis, D. Leščinskas, G. Mattogno, L. Stakvilevičius, G. Treideris, and S. Viticoli, J. Appl. Phys. **76** 5738 (1994).

[21] B. W. Kim and A. Majerfeld, J. Appl. Phys. **77**, 4552 (1995).

[22] E. Pelvé, F. Beltram, C. G. Bethea, B. F. Levine, V. O. Shen, S. J. Hsieh, and R. R. Abbott, J. Appl. Phys. **66**, 5656 (1989).

[23] S. R. Andrews and B. A. Miller, J. Appl. Phys. **70**, 993 (1991).

[24] H. C. Liu, A. G. Steele, M. Buchanan, and Z. R. Wasilewski, J. Appl. Phys. **73**, 2029 (1993).

[25] K. L. Tsai, C. P. Lee, K. H. Chang, D. C. Liu, H. R. Chen, and J. S. Tsang, Appl. Phys. Lett. **64**, 2436 (1994).

[26] C. Y. Lee, M. Z. Tidrow, K. K. Choi, W. H. Chang, and L. F. Eastman, appl. Phys. Lett. **65**, 442 (1994).

[27] P. Man and D. S. Pan, Appl. Phys. Lett. **66**, 192 (1995).

[28] H. C. Liu, Appl. Phys. Lett. **60**, 1507 (1992).

[29] Aldert van der Ziel, *Noise in Solid State Devices and Circuits* (Wiley-Interscience, New York, 1986).

[30] Alder van der Ziel, *Noise in Measurements* (Wiley-Interscience, New York 1976).

[31] Daniel C. Wang, Gijs Bosman, and Sheng S. Li, Appl. Phys. Lett. **65**, 183 (1994).

[32] Daniel C. Wang, Gijs Bosman, Yeng H. Wang, and Shneg S. Li, J. Appl. Phys. **77**, 1107 (1995).

[33] Daniel C. Wang, Gijs Bosman, and Sheng S. Li, J. Appl. Phys. **79**, 1486 (1996).

[34] S. M. Sze, *Physics of Semiconductor Devices* 2nd Ed. (Wiley-Interscience, New York, 1981).

[35] W. Shockley, *Electrons and Holes in Semiconductors* (D. Van Nostrand, Princeton, N.J., 1950).

[36] J. A. Brum and G. Bastard, Phys. Rev. B **30** 905 (1984).

[37] A. Rose, *Concepts in Photoconductivity and Allied Problems* (Wiley-Interscience, New York, 1963).

[38] H. C. Liu, Appl. Phys. Lett. **61**, 2703 (1992).

[39] B. Xing, H. C. Liu, P. H. Wilson, M. Buchanan, Z. R. Wasilewski, and J. G. Simmons, J. Appl. Phys. **76**, 1889 (1994).

[40] W. A. Beck, Appl. Phys. Lett. **63**, 3589 (1993).

[41] K. K. Choi, Appl. Phys. Lett. **65**, 1226 (1994).

[42] V. D. Shadrin, V. V. Mitin, V. A. Kochelap, and K. K . Choi, J. Appl. Phys. **77**, 1771 (1995).

[43] A. K. Ghatak, K. Thyagarajan, and M. R. Shenoy, IEEE J. Quantum Electron. **QE-24**, 1524 (1988).

[44] K. M. S. V. Bandara, D. D. Coon, Byungsung O, Y. F. Lin, and M. H. Francombe, Appl. Phys. Lett. **53**, 1931 (1988).

[45] J. W. Choe, Byungsung, K. M. S. V. Bandara, and D. D. Coon, Appl. Phys. Lett. **56**, 1679 (1990).

[46] J. S. Parker and G. Bosman, IEEE Trans. Electron Devices **39**, 1282 (1992).

[47] C. F. Gerald and P. O. Wheatley, *Applied Numerical Analysis*, 3rd edition (Addison-Wesley, New York 1984).

[48] H. Nyquist, Phys. Rev. **32**, 110 (1928).

[49] R. H. Bube, *Electronic Properties of Crystalline Solids* (Academic Press, New York, 1974).

[50] Yeng-Cheng Wang and Sheng S. Li, J. Appl. Phys., **74**, 2192 (1994).

[51] Yeng-Cheng Wang and Sheng S. Li, J. Appl. Phys., **75**, 582 (1994).

[52] Y. C. Wang and S. S. Li, J. Appl. Phys., **75**, 8168 (1994).

[53] R. C. Jones, *Advances in Electronics* L. Marton, Ed. (Academic Press, New York, 1953).

[54] W. Heitler, *The Quantum Theory of Radiation* 3rd Ed. (Oxford University Press, London 1954).

[55] Y. Fu and M. Willander, J. Appl. Phys. **77**, 4648 (1995).

[56] S. Datta, *Quantum Phenomena* (Addison-Wesley, New York 1989).

[57] L. J. Kozlowski, G. M Williams, R. E. DeWames, K. Vural, V. Swaminathan, J. W. Stayt Jr., K. G. Glogovsky, R. E. Leibenguth, L. E. Smith, and W. A. Gault, ECS Proc. **94-5**, 5 (1994).
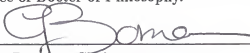
[58] W. A. Beck, T. S. Faska, J. W. Little, A. C. Goldberg, J. Albritton, and M. Sensiper, ECS Proc. **95-28**, 7 (1995).

[59] S. D. Gunapala, J. K. Liu, M. Sundaram, J. S. Park, C. A. Shott, T. Hoelter, T. L. Lin, S. T. Massie, P. D. Maker, R. E. Muller, and G. Sarusi, ECS Proc. **95-28**, 55 (1995).

BIOGRAPHICAL SKETCH

Daniel Chien Wang was born in Tainan, Taiwan, R. O. C., on November 30, 1965. He received the B.S. degree in the Department of Electrical Engineering of the National Central University in 1988. After his graduation, he served in the Chinese Army for two years. From 1990 to 1991, he was a research assistant of Professor P. K. Tseng in the Physics Department of the National Taiwan University.

On August 1991, he went to University of Florida to start his graduate program. He received the M.S. degree at the Department of Electrical Engineering with a thesis entitled: "The Noise Performance of Bound-to-Miniband Transition III-V Quantum Well Infrared Photodetectors". After his graduation, he extended his research and continued working towards his Ph.D. degree. His Ph.D. research has been focused on the semiconductor noise characterization and device modelling of both n-type and p-type quantum well infrared photodetectors.
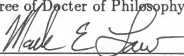
I certify that I have read this study and that in my opinion it conforms to acceptable standards of scholarly presentation and is fully adequate, in scope and quality, as a dissertation for the degree of Docter of Philosophy.

Gijs Bosman, Chairman
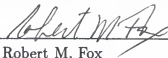Professor of Electrical and Computer Engineering

I certify that I have read this study and that in my opinion it conforms to acceptable standards of scholarly presentation and is fully adequate, in scope and quality, as a dissertation for the degree of Docter of Philosophy.

Sheng S. Li
Professor of Electrical and Computer Engineering

I certify that I have read this study and that in my opinion it conforms to acceptable standards of scholarly presentation and is fully adequate, in scope and quality, as a dissertation for the degree of Docter of Philosophy.

Mark E. Law
Associate Professor of Electrical and
Computer Engineering

I certify that I have read this study and that in my opinion it conforms to acceptable standards of scholarly presentation and is fully adequate, in scope and quality, as a dissertation for the degree of Docter of Philosophy.

Robert M. Fox
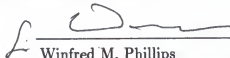Associate Professor of Electrical and
Computer Engineering

I certify that I have read this study and that in my opinion it conforms to acceptable standards of scholarly presentation and is fully adequate, in scope and quality, as a dissertation for the degree of Docter of Philosophy.

Christopher J. Stanton
Professor of Physics

This dissertation was submitted to the Graduate Faculty of the College of Engineering and to the Graduate School and was accepted as partial fulfillment of the requirements for the degree of Docter of Philosophy.

August 1996

Winfred M. Phillips
Dean, College of Engineering

Karen A. Holbrook
Dean, Graduate School